Supporting Information

Highly crystalline low-bandgap polymer nanowires towards high-performance thick-film organic solar cells exceeding 10% power conversion efficiency

Jaewon Lee,† Dong Hun Sin,† Byungho Moon, Jisoo Shin, Heung Gyu Kim, Min Kim, and Kilwon Cho*

Department of Chemical Engineering, Pohang University of Science and Technology, Pohang 790-784, Korea. E-mail: kwcho@postech.ac.kr

I. Experimental section

1. Materials and Methods:

Materials All reagents and chemicals were purchased from commercial sources and used without further purification. All anhydrous organic solvents for the synthesis, characterization, and device fabrication steps were purchased from Sigma-Aldrich and TCI. [6,6]-Phenyl-C_{71}-butyric acid methyl ester ($PC_{71}BM$) was obtained from Nano-C. 3,3'-difluoro-5,5'-bis(trimethylstannyl)-2,2'-bithiophene,[1] dibromonaphtho[1,2-c:5,6-c′]bis[1,2,5]thiadiazole and 4,9-bis(5-bromo-4-(2-decyltetradecyl)thiophen-2-yl)naphtho[1,2-*c*:5,6*c*′]bis[1,2,5]thiadiazole,[2] 3-(2-octyldodecyl)-5-trimethylstannylthiophene and 3-(2-decyltetradecyl)-5-trimethylstannylthiophene,[3] 4,7-Bis(5-bromo-4-(2-decyltetradecyl)thiophen-2-yl)-5,6-difluoro[2,1,3]benzothiadiazole[4] were synthesized using modified literature procedure.

Characterizations of compounds ^1H and ^{13}C NMR spectra of intermediate monomers were recorded on a Bruker AVANCE 400 MHz NMR spectrometer in deuterated chloroform

solution ($CDCl_3$) with 0.003%TMS as internal reference. P4TNTz-2F polymers were characterized by ^1H NMR (500 MHz) on Bruker DRX 500 spectrometer in 1,2-dichlorobenzene-d_4 at 110 °C. Elemental analysis was performed by Vario MICRO. TGA plots were measured with a TA Instruments, Inc., TGA 2050 under a nitrogen atmosphere at heating and cooling rates of 10 °C·min^{-1}. Differential scanning calorimetry (DSC) analysis was performed on a TA Instruments Q100 under flowing N_2 at a heating rate of 5 °C·min^{-1}. Number-average (M_n) and weight-average (M_w) molecular weights were determined with gel permeation chromatography (PL-GPC 220 High Temperature GPC, Agilent Technologies) in 1,2,4-trichlorobezene at 160 °C, using two PL mixed B columns (7.2 × 300 mm) in series, and calibrated against narrow polydispersity polystyrene standards. Atomic force microscopy (AFM) and transmission electron microscopy (TEM) images were obtained using a MultiMode 8 Scanning Probe Microscope VEECO Instruments Inc. and JEOL JEM-2200FS (with Image Cs-corrector), respectively.

Electrochemical characterizations The electrochemical cyclic voltammetry (CV) was conducted on a PowerLab/AD instrument model system with glassy carbon disk, Pt wire, and Ag/Ag+ electrode as the working electrode, counter electrode, and reference electrode, respectively in a 0.1 M tetrabutylammonium hexafluorophosphate (n-Bu_4NPF_6)-anhydrous acetonitrile solution at a potential scan rate of 50 mV s^{-1}. Thin films of samples were deposited onto the glassy carbon working electrode from a 1.5 mg mL^{-1} hot chlorobenzene solution. The electrochemical onsets were determined at the position where the current starts to differ from the baseline. The potential of Ag/AgCl reference electrode was internally calibrated by using the ferrocene/ferrocenium redox couple (Fc/Fc^+). The electrochemical energy levels were estimated by using the empirical formula: $E_{HOMO} = -(4.80 + E_{onset,\ ox})$ and $E_{LUMO} = -(4.80 + E_{onset,\ red})$.[5] UV-vis spectra were recorded on a Varian CARY-5000 UV-vis spectrophotometer. For the measurements of thin films, materials were spun coated onto precleaned glass substrates from hot chlorobenzene solutions (10 mg mL^{-1}). Optical band gap (E_g^{opt}) was determined from the absorption edge of thin film sample.

Computational studies Density functional theory (DFT) calculations were performed to facilitate an in-depth understanding of the electronic structure and molecular conformation of the polymer by Gaussian 09 software package.[6] Hybrid three-parameter B3LYP functional combined with 6-31G(d) basis set was used to obtain the optimized structures at the singlet ground state.[7] For simplicity, the alkyl chains were trimmed with methyl chains. The highest

occupied molecular orbital (HOMO) as well as lowest unoccupied molecular orbital (LUMO) energy levels were analyzed using minimized singlet geometries to approximate the ground state.

Grazing incidence wide angle X-ray diffraction (GIXD) analysis 2D GIXD measurements were performed using Beamline 9A at the Pohang Accelerator Laboratory (PAL). The photon energy is 10.6408 keV (λ = 1.1651 Å). The GIWAXS images shown are normalized with respect to exposure time and film thickness.

PFET fabrication and measurements Polymer field-effect transistor (PFET) devices were prepared on an octadecyltrimethoxysilane (OTS)-treated surface prepared from a highly doped *p*-Si wafer with a 300 nm-thick thermally grown oxide layer. The wafer served as a gate electrode, whereas the oxide layer acted as the gate dielectric (capacitance = 10.8 nF cm^{-2}). The SI/SiO_2 wafers were cleaned with piranha solution (a mixture of 70 vol% H_2SO_4 and 30 vol% H_2O_2), followed by UV-ozone treatment. The surface of the wafers was modified with OTS self-assembled monolayers by using dipping method about 20 min, and then the samples were kept overnight in a vacuum desiccator. Then the semiconducting polymers were spin-coated on the substrates at 3000 rpm for 60s from a 0.5 wt% chlorobenzene solution (~40 nm in thickness) and dried in a vacuum desiccator overnight. After carrying out thermal annealing for 30 min in a N_2 atmosphere, source and drain electrodes (Au 80 nm) were thermally evaporated through shadow mask to define channel length and width, 100 μm and 1000 μm, respectively.

The electrical properties of the PFET devices were characterized at room temperature in a dark environment under vacuum condition using a Keithley 4200-SCS semiconductor parametric analyzer. The field-effect mobility (μ) and the threshold voltage (V_T) were estimated in the saturation regime (V_{DS} = -60 V) with the following equation[8]: $I_D = (W/2L)\ \mu C_g\ (V_{GS} - V_T)^2$, where I_D is the drain current, C_g is the capacitance of the gate dielectric and V_{GS} is the gate-source voltage.

Fabrication and characterization of organic solar cell (OSC) devices The inverted structure of the OPV devices was prepared with a configuration of indium tin oxide (ITO) (110nm) / zinc oxide (ZnO) (30nm)/polymer:$PC_{71}BM$/MoO_3 (7nm)/Au (90nm). ITO-coated glass substrates were cleaned by sequential sonications with detergent, distilled water, acetone, and isopropyl alcohol for 15 min at each step. After UV-ozone treatment for 30 min, a ZnO electron

transport layer[9] was prepared by spin-coating ZnO nanoparticle dispersion (in 1-buthanol) at 4000 rpm and then dried under low vacuum (<10^{-2} Torr) for 2 h. Active layer solutions were prepared in CB (polymer concentration: 15 mg mL^{-1}) and kept on hotplate at an elevated temperature (70 °C) for more than 6 h in a N_2 glovebox. Active layers were spin-coated from the warm polymer solution on the prepared ZnO/ITO/glass substrate in a N_2 glovebox. To deposit the electrodes, the samples were transferred into a vacuum chamber (pressure < 4×10^{-6} Torr), and then MoO_3 (7nm)/Au (90nm) were deposited sequentially on top of the active layer by thermal evaporation. The electrical characteristics were measured with a source/measure unit (Keithley 4200) under 100 mW cm^{-2} AM1.5 solar illumination in a N_2-filled glove box. Light was generated with an Oriel 1-kW solar simulator referenced using a Reference Cell PVM 132 calibrated at the US National Renewable Energy Laboratory. A photomodulation spectroscopic set-up (model Merlin, Oriel) was used to measure the incident photon-to-current conversion efficiency (IPCE) as a function of light wavelength. The device area was 0.0555 cm^2.

SCLC measurement The hole and electron mobility data was extracted from the dark *J–V* characteristics of hole-only devices, ITO/MoO_3/P4TNTz-2F:$PC_{71}BM$/MoO_3/Au and electron-only devices, Al/P4TNTz-2F:$PC_{71}BM$/LiF/Al. The electrical characteristics were measured with a source/measure unit (Keithley 4200) in a N_2-filled glove box. The dark *J–V* curves were fitted by using the Mott-Gurney square law[10] $J = (9/8)\varepsilon\mu(V^2/L^3)$, where ε is the static dielectric constant of the medium and μ is the carrier mobility.

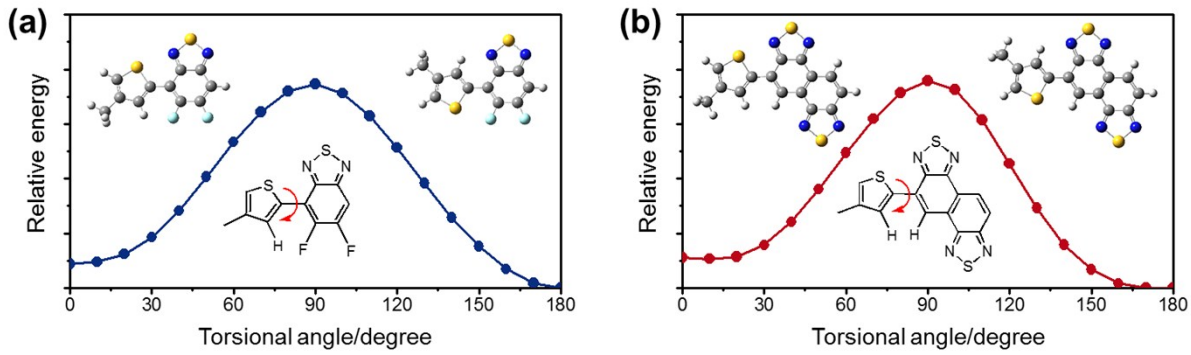

Fig. S1 DFT calculated relative energy of (a) **1T-2FBT** and (b) **1T-NTz** conformers with different dihedral angles between the **2FBT**/**NTz** unit and one of the adjacent methyl-thiophene.

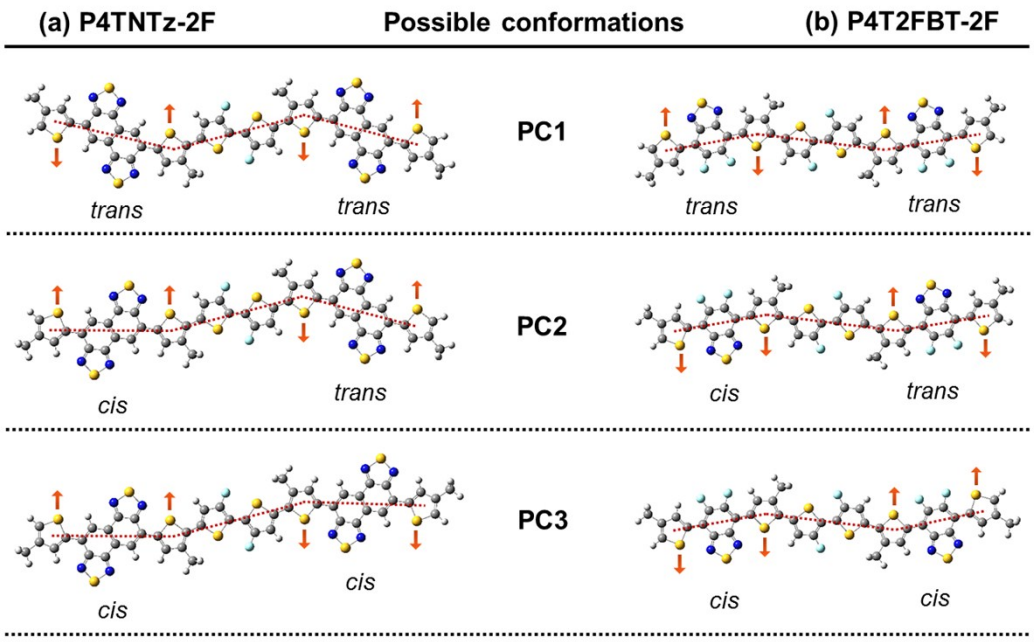

Fig. S2 Illustration of possible conformations of P4TNTz-2F and P4T2FBT-2F model molecules. The arrows represent the sulfur atom directions. Density functional theory (DFT) calculation, using B3LYP/6-31G* model as implemented in GAUSSIAN 09, was performed on the model molecules.

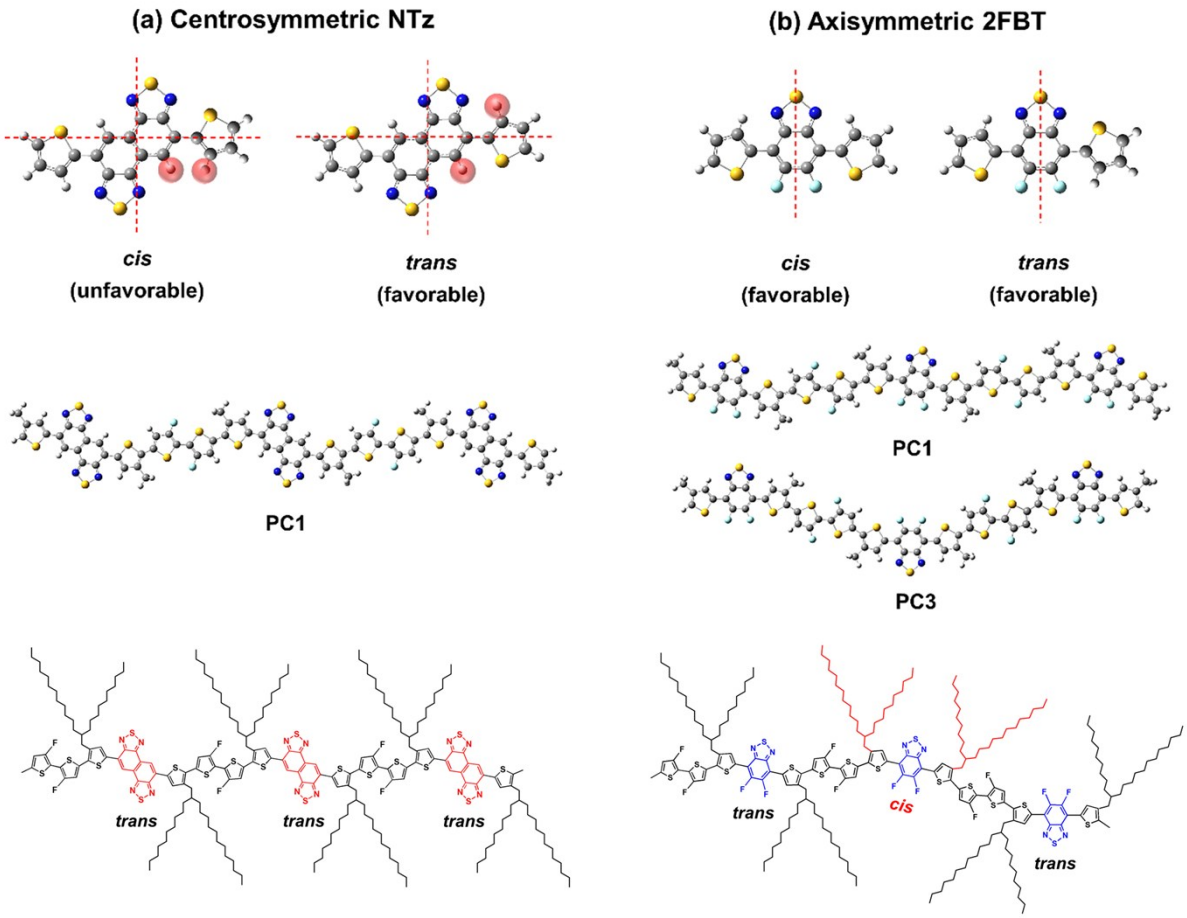

Fig. S3 Illustration of optimized backbone conformations and side chain arrangements of (a) P4TNTz-2F and (b) P4T2FBT-2F as calculated at the B3LYP/6-31G(d) level.

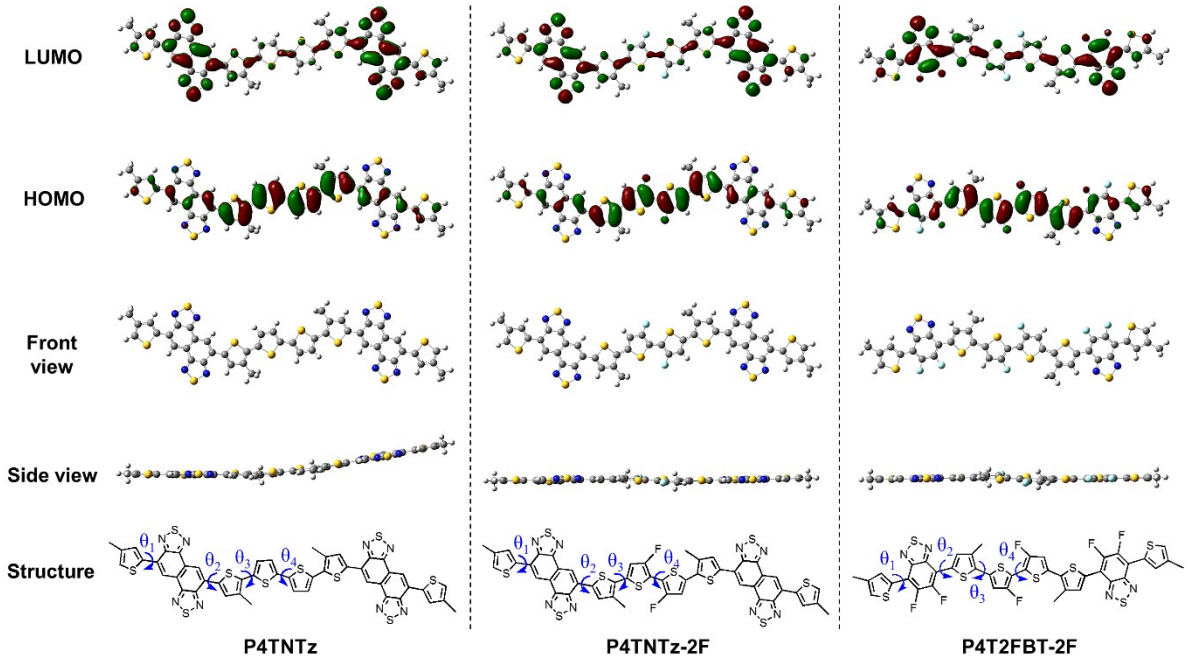

Fig. S4 HOMO/LUMO orbital distributions and molecular conformations as calculated at the B3LYP/6-31G(d) level, and chemical structures of P4TNTz, P4TNTz-2F, and P4T2FBT-2F based model compounds.

Table S1 Torsional angles and energy levels of model compounds calculated by DFT.

Polymer	θ_1 [deg]	θ_2 [deg]	θ_3 [deg]	θ_4 [deg]	HOMO [eV]	LUMO [eV]
P4TNTz	1.88	4.49	10.37	11.95	-4.83	-2.98
P4TNTz-2F	1.14	3.57	8.16	0.03	-4.87	-3.02
P4T2FBT-2F	0.22	0.19	7.79	0.02	-4.87	-2.88

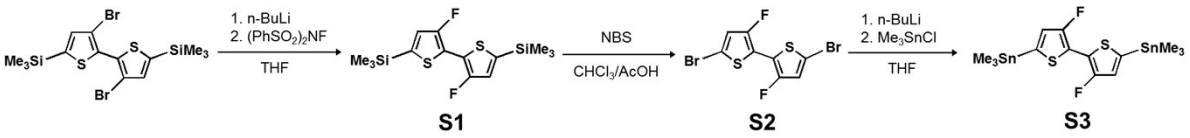

Scheme S1 Synthetic procedure of 5,5′-bis(trimethylstannyl)-3,3′-difluoro-2,2′-bithiophene.

5,5′-Bis(trimethylsilyl)-3,3′-difluoro-2,2′-bithiophene (S1). A solution of 5,5′-bis(trimethylsilyl)-3,3′-dibromo-2,2′-bithiophene (1.0 g, 2.1 mmol) in anhydrous THF (20 mL) was cooled to −78 °C under N_2. 2.5 M of n-BuLi in hexane (1.9 mL, 4.7 mmol) was added dropwise and the mixture was stirred for 1h. The solution was further stirred for 30 min at room temperature. The solution was then cooled to −78 °C again before *N*-fluorobenzenesulfonimide ($(PhSO_2)_2NF$) (1.6 g, 5.1 mmol) in THF (5 mL) was added. The reaction mixture was warmed up to room temperature and stirred overnight, and then poured into water and extracted with dichloromethane for three times (30 ml×3). The organic layer was dried over Na_2SO_4 and concentrated in vacuum. The residue was purified by silica gel column chromatography (*n*-hexane) to afford the product as a white solid (0.58 g, 78%).

^{1}H NMR (400MHz, $CDCl_3$, ppm): δ 6.96 (s, 2H), 0.32 (s, 12H).

5,5′-Dibromo-3,3′-difluoro-2,2′-bithiophene (S2). To a solution of compound **S1** (0.5 g, 1.4 mmol) in chloroform/acetic acid (10/10 mL) was added portionwise *N*-bromosuccinimide (NBS) (0.59 g, 3.3 mmol) in the dark. After stirring overnight at 60 °C, the reaction mixture was poured into water and extracted with dichloromethane for three times (30 ml×3). The organic layer was dried over Na_2SO_4 and concentrated in vacuum. The residue was purified by silica gel column chromatography (*n*-hexane) and recrystallized from acetonitrile to afford the product (0.42 g, 81%).

^{1}H NMR (400MHz, $CDCl_3$, ppm): δ 6.87 (s, 2H).

5,5′-Bis(trimethylstannyl)-3,3′-difluoro-2,2′-bithiophene (S3). To a solution of compound **S2** (1.2 g, 3.33 mmol) in anhydrous THF (15 mL) was cooled to −78 °C under N_2. 2.5 M of n-BuLi in hexane (3 mL, 7.5 mmol) was added dropwise and the mixture was stirred for 1.5h. 1 M of trimethyltin chloride in hexane (8.3 mL, 8.3 mmol) was added and the reaction mixture was warmed up to room temperature and then stirred overnight. The resulting mixture was poured into water and extracted with dichloromethane for three times (30 ml×3). The organic layer was dried over Na_2SO_4 and concentrated in vacuum. The residue was recrystallized from

methanol to afford the product (1 g, 57%).

^{1}H NMR (400MHz, $CDCl_3$, ppm): δ 6.89 (t, 2H), 0.39 (m, 12H). ^{13}C NMR (100 MHz, $CDCl_3$, ppm): δ 155.18, 138.20, 123.31, 116.76, −0.38.

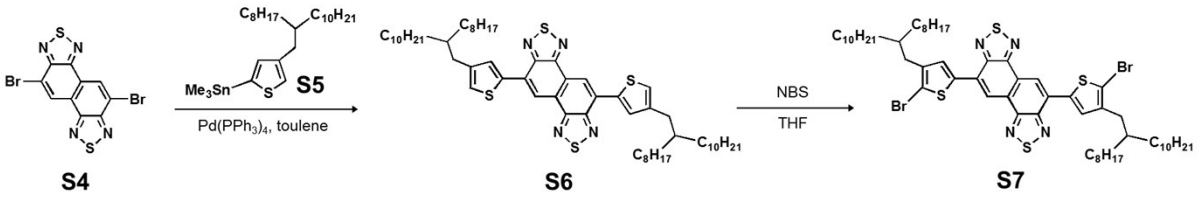

Scheme S2 Synthetic procedure of NTz monomer with 2-octyldodecyl (OD) alkyl chain.

4,9-Bis(4-(2-octyldodecyl)thiophen-2-yl)naphtho[1,2-c:5,6-c′]-bis[1,2,5]thiadiazole (S6). A mixture of **S4** (402 mg, 1.0 mmol), **S5** (1.16 g, 2.2 mmol) and $Pd(PPh_3)_4$ (57 mg, 0.05 mmol) in toluene (30 mL) was heated to 100 °C for 20 h under N_2. After the mixture cooled to room temperature, aqueous KF was added, and the mixture was extracted with dichloromethane for two times (30 ml×2). The organic layer was washed with brine and then dried over Na_2SO_4 and concentrated in vacuum. The residue was purified by silica gel column chromatography (*n*-hexane/dichloromethane, 8/2) to afford the product as a red solid (775 mg, 80%).

^{1}H NMR (400MHz, $CDCl_3$, ppm): δ 8.96 (s, 2H), 8.11 (d, 2H), 7.10 (d, 2H), 2.66 (d, 4H), 1.75 (m, 2H), 1.13−1.43 (m, 64H), 0.80−0.90 (m, 12H).

4,9-Bis(5-bromo-4-(2-octyldodecyl)thiophen-2-yl)naphtho[1,2-c:5,6-c′]bis[1,2,5]thiadiazole (S7). To a solution of compound **S6** (484 mg, 0.5 mmol) in 50 mL of THF at room temperature, NBS (187 mg, 1.05 mmol) was added portionwise. After the mixture was stirred for 6 h at room temperature, $NaHCO_3$ solution was added, and the mixture was extracted with dichloromethane for two times (30 ml×2). The organic layer was washed with brine and then dried over Na_2SO_4 and concentrated in vacuum. The residue was purified by silica gel column chromatography (*n*-hexane/dichloromethane, 8/2) to afford the product as a red solid (423 mg, 75%).

^{1}H NMR (400MHz, $CDCl_3$, ppm): δ 8.95 (s, 2H), 7.92 (s, 2H), 2.61 (d, 4H), 1.80 (br, 2H), 1.11−1.46 (m, 64H), 0.78−0.91 (m, 12H).

^{13}C NMR (100 MHz, $CDCl_3$): δ 153.1, 152.0, 142.3, 137.9, 129.4, 125.8, 124.6, 121.4, 113.3, 38.6, 34.4, 33.4, 31.9, 30.1, 29.7, 29.7, 29.4, 26.6, 22.6, 14.1.

Elem. Anal. Calcd for ($C_{58}H_{86}N_4S_4Br_2$): C, 61.79; H, 7.69; N, 4.97. Found: C, 61.71; H, 7.61;

N, 4.95.

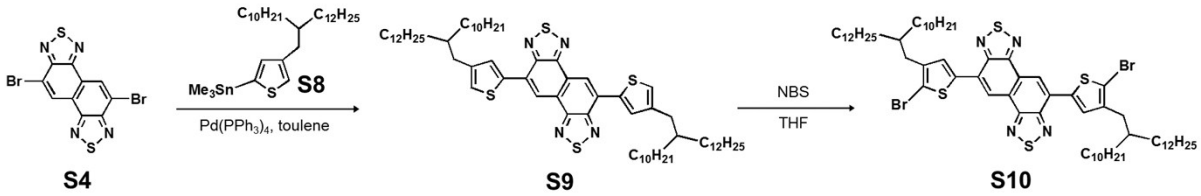

Scheme S3 Synthetic procedure of NTz monomer with 2-decyltetradecyl (DT) alkyl chain.

4,9-Bis(4-(2-decyltetradecyl)thiophen-2-yl)naphtho[1,2-c:5,6-c′]-bis[1,2,5]thiadiazole (S9). A similar procedure was performed with **S6**. The product was obtained as a red solid (389 mg, 72%).

^{1}H NMR (400MHz, $CDCl_3$, ppm): δ 8.99 (s, 2H), 8.12 (d, 2H), 7.11 (d, 2H), 2.66 (d, 4H), 1.79 (br, 2H), 1.12−1.45 (m, 80H), 0.79−0.91 (m, 12H).

4,9-Bis(5-bromo-4-(2-decyltetradecyl)thiophen-2-yl)naphtho[1,2-c:5,6-′]bis[1,2,5]thiadiazole (S10). A similar procedure was performed with **S7** and the product was obtained as a red solid (477 mg, 77%).

^{1}H NMR (400MHz, $CDCl_3$, ppm): δ 8.83 (s, 2H), 7.88 (s, 2H), 2.60 (d, 4H), 1.80 (br, 2H), 1.15−1.48 (m, 80H), 0.79−0.91 (m, 12H).

^{13}C NMR (100 MHz, $CDCl_3$): δ 153.3, 152.1, 142.4, 137.9, 129.4, 125.9, 124.7, 121.5, 113.3, 38.6, 34.3, 33.4, 31.9, 30.1, 30.1, 29.7, 29.7, 29.7, 29.7, 29.4, 26.6, 22.7, 14.1.

Elem. Anal. Calcd for ($C_{66}H_{104}N_4S_4Br_2$): C, 63.95; H, 8.29; N, 4.52. Found: C, 63.81; H, 8.12; N, 4.53.

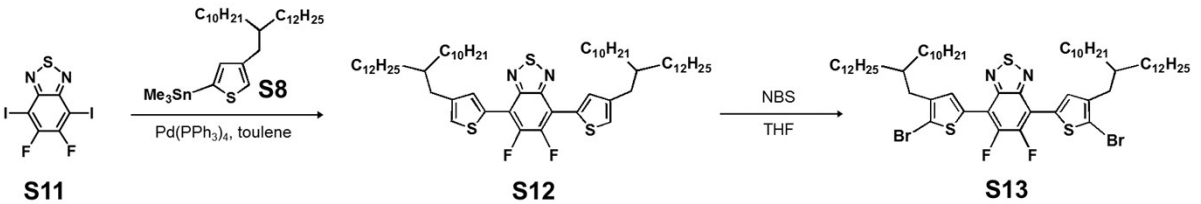

Scheme S4 Synthetic procedure of 2FBT monomer with 2-decyltetradecyl (DT) alkyl chain.

4,7-Bis(5-bromo-4-(2-decyltetradecyl)thiophen-2-yl)-5,6-difluoro[2,1,3]benzothiadiazole (S13) was synthesized according to the literature procedure.[4]

^{1}H NMR (400MHz, $CDCl_3$, ppm): δ 7.92 (s, 2H), 2.59 (d, 4H), 1.73 (s, 2H), 1.35-1.18 (m, 80H), 0.86 (m, 12H).

^{13}C NMR (100 MHz, $CDCl_3$, ppm): δ 151.09, 150.88, 148.50, 148.46, 148.41, 148.30, 141.81, 132.44, 132.39, 132.35, 131.06, 131.04, 115.15, 115.12, 115.08, 111.12, 111.07, 111.02, 110.96, 38.55, 34.16, 33.40, 31.96, 30.03, 29.73, 29.68, 29.39, 26.63, 22.71, 14.13.

Elem. Anal. Calcd for $C_{62}H_{100}Br_2F_2N_2S_3$: C, 63.78; H, 8.63; N, 2.40. Found: C, 63.67; H, 8.71; N, 2.35.

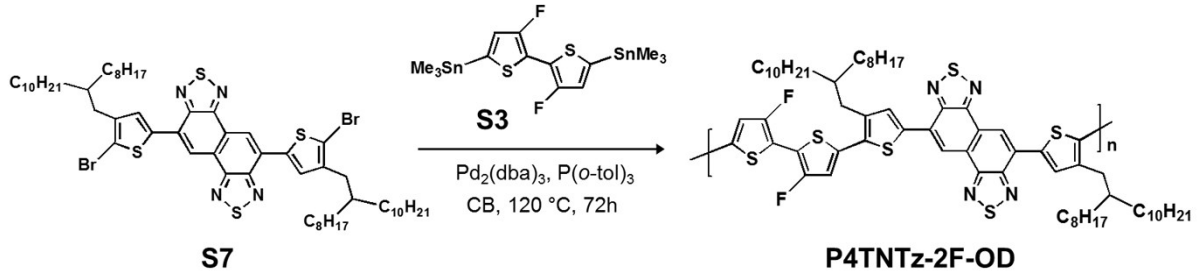

Scheme S5 Synthetic procedure of P4TNTz-2F-OD.

P4TNTz-2F-OD. Compound **S7** (338 mg, 0.3 mmol), **S3** (158.2 mg, 0.3 mmol), $Pd_2(dba)_3$ (8.5 mg), P(*o*-tol)$_3$ (12.5 mg), and dry chlorobenzene (10 mL) were added to a flame-dried and nitrogen-filled one-neck round-bottom flask (25 mL). The flask was purged with N_2 for 20 min and the reactant was heated to 120 °C for 6 h. Note that the reaction was terminated without end-capping because the polymer was precipitated during the polymerization reaction. The mixture was cooled to a room temperature and added dropwise to methanol (300 mL) to obtain a precipitate. After stirring for several hours, the resultant polymer was collected by filtration and loaded into an extraction thimble, which was then subjected to Soxhlet extraction with methanol, acetone, *n*-hexane, chloroform, and chlorobenzene. Polymer was recovered from the chlorobenzene fraction by rotary evaporation and then precipitated in methanol. The precipitates were collected and dried under vacuum at 40 °C for 24 h to afford the polymer as a black solid (298.3 mg, 85%).

GPC (1,2,4-trichlorobenzene, 160 °C): M_n = 13.8 kDa; M_w/M_n (PDI) = 1.88.

Elem. Anal. Calcd for $(C_{66}H_{90}F_2N_4S_6)_n$: C, 67.76; H, 7.75; N, 4.79. Found: C, 67.64; H, 7.71; N, 4.74.

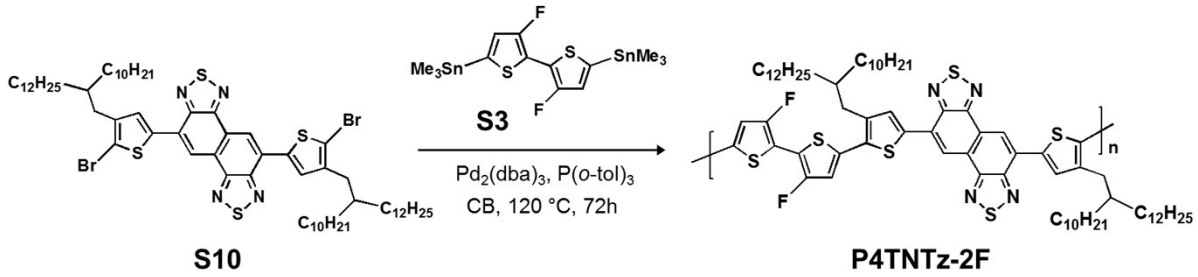

Scheme S6 Synthetic procedure of P4TNTz-2F.

P4TNTz-2F. A similar procedure with P4TNTz-2F-OD was performed for P4TNTz-2F. The reaction time of polymerization was controlled to afford P4TNTz-2F polymers with various molecular weights (The reaction time was 24h, 48h, and 72h for low-molecular weight, medium-molecular weight, and high-molecular weight, respectively). After adding trimethylthienyltin (0.15 equiv.) to the reaction flask, the reaction was kept at 120 °C for an additional 3 h. 2-Bromothiophene (0.5 equiv.) was then added to the reaction flask, and the temperature was kept at 120 °C for an additional 5 h to complete the end-capping reaction. Soxhlet extraction was conducted with methanol, acetone, *n*-hexane, chloroform, chlorobenzene, and *o*-dichlorobenzene. Polymers were recovered from the chloroform (low-M_n), chlorobenzene (medium-M_n), and *o*-dichlorobenzene (high-M_n) fractions afford the polymers as black solids.

^{1}H NMR (500MHz, *o*-dichlorobenzene-d4, 383K, ppm): δ 9.11 (s, 2H), 8.35 (s, 2H), 7.13 (s, 2H), 3.00 (d, 4H), 2.06 (br, 2H), 1.20−1.55 (m, 80H), 0.78−0.91 (m, 12H). (*The results of ^{1}H NMR analysis, presented here, are for the chloroform fraction (low-M_n) because the low-M_n P4TNTz-2F provided a more clear spectra among the different M_n polymers at 383K).

GPC #1 (1,2,4-trichlorobenzene, 160 °C): M_n = 11.8 kDa; M_w/M_n = 2.24 for low-M_n. M_n = 18.3 kDa; M_w/M_n = 1.85 for medium-M_n. M_n = 29.3 kDa; M_w/M_n = 2.29 for high-M_n.

GPC #2 (chlorobenzene, 60 °C): M_n = 91.5 kDa; M_w/M_n = 3.02 for low-M_n. M_n = 124.0 kDa; M_w/M_n = 3.75 for medium-M_n. High-M_n is not available because of its poor solubility to process GPC measurement at 60 °C.

Elem. Anal. Calcd for $(C_{74}H_{106}F_2N_4S_6)_n$: C, 69.33; H, 8.33; N, 4.37. Found: C, 69.11; H, 8.27; N, 4.32. (*Elemental analysis was conducted for the chlorobenzene fraction (medium-M_n)).

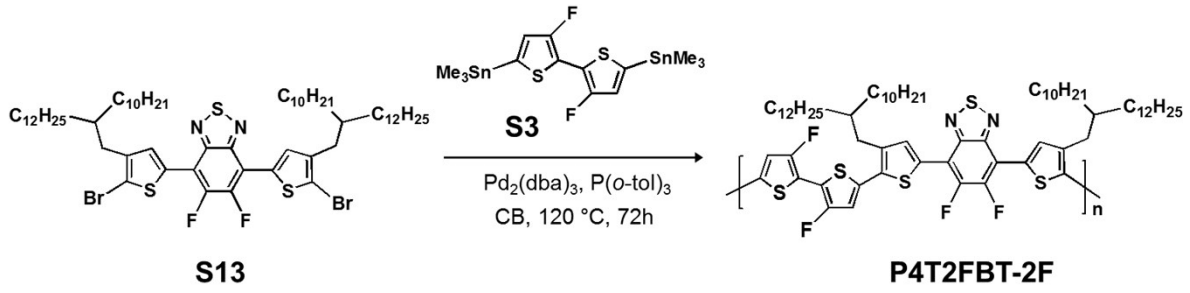

Scheme S7 Synthetic procedure of P4T2FBT-2F.

P4T2FBT-2F. A similar procedure with P4TNTz-2F-OD was performed for P4T2FBT-2F. The flask was purged with N_2 for 20 min and the reactant was heated to 120 °C for 2d. Soxhlet extraction was conducted with methanol, acetone, *n*-hexane, and chloroform. Polymer was recovered from the chloroform fraction by rotary evaporation and then precipitated in methanol. The precipitates were collected and dried under vacuum at 40 °C for 2 d to afford the polymer as a dark green solid (240.7 mg, 77%).

GPC (1,2,4-trichlorobenzene, 160 °C): M_n = 17.3 kDa; M_w/M_n = 1.75.

Elem. Anal. Calcd for $(C_{70}H_{104}F_4N_2S_5)_n$: C, 69.49; H, 8.66; N, 2.32. Found: C, 69.27; H, 8.53; N, 2.27.

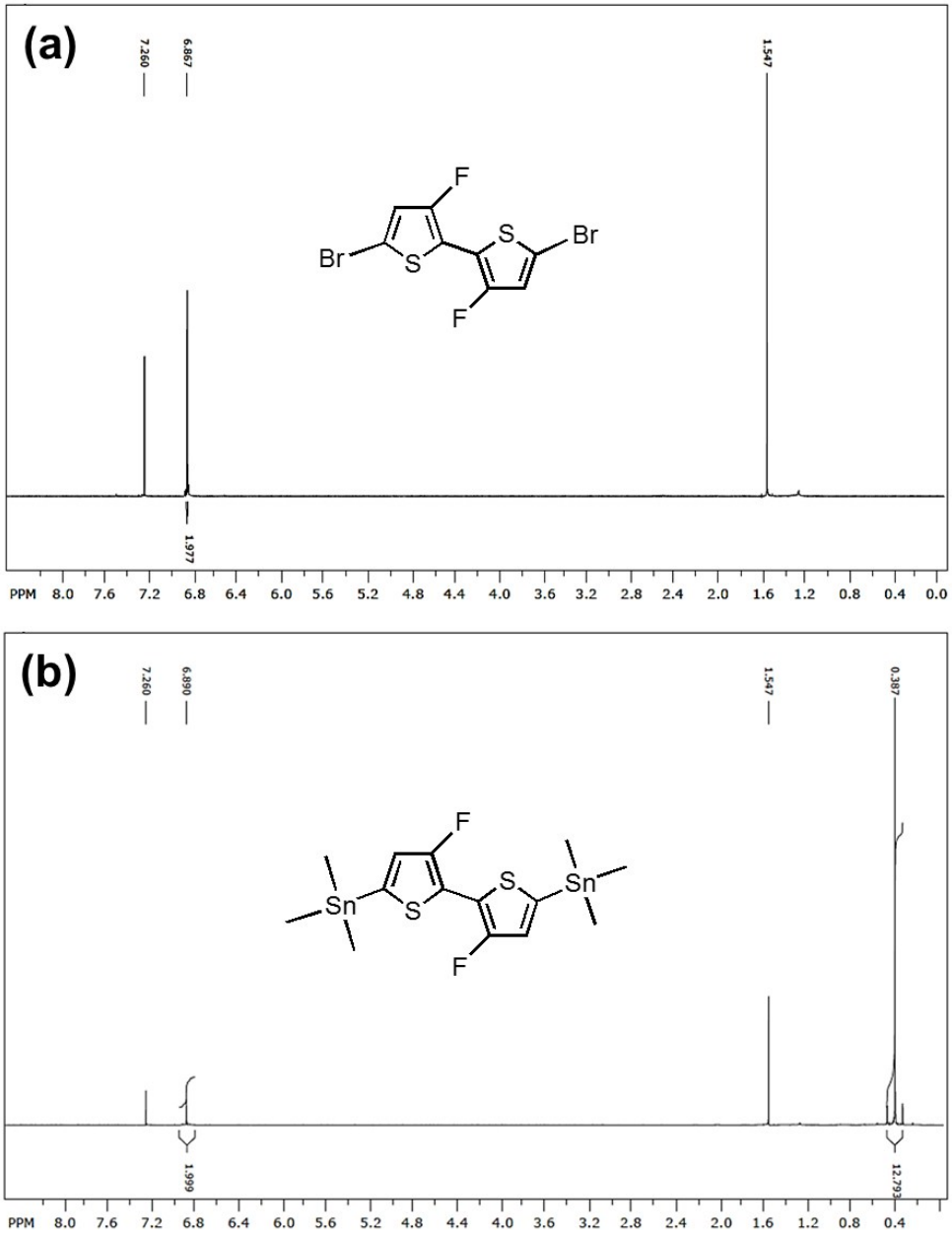

Fig. S5 ^{1}H NMR (400 MHz, chloroform-d) spectra of (a) 5,5′-dibromo-3,3′-difluoro-2,2′-bithiophene and (b) 5,5′-bis(trimethylstannyl)-3,3′-difluoro-2,2′-bithiophene monomer at 298K.

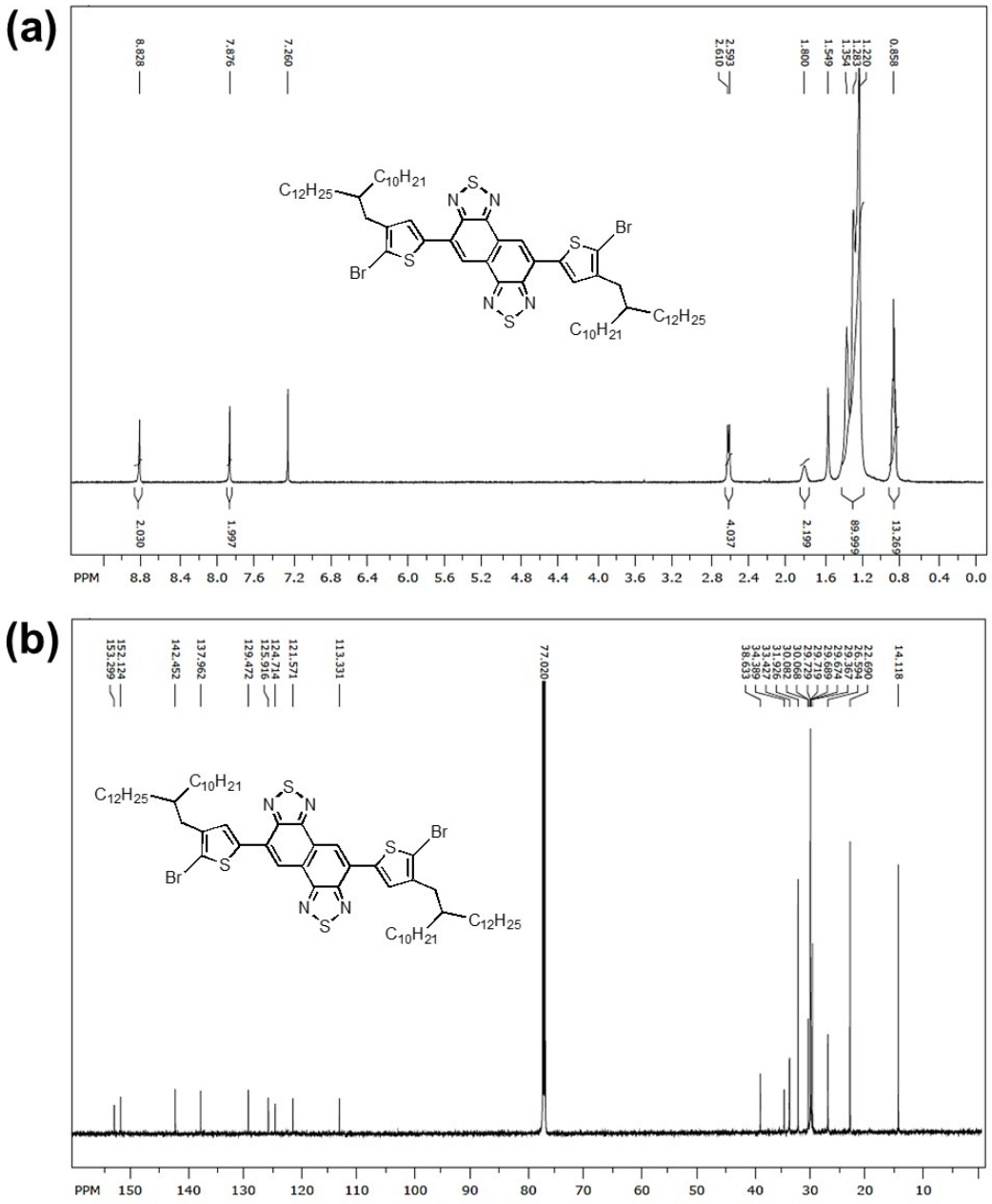

Fig. S6 (a) ^{1}H NMR (400 MHz, chloroform-d) and (b) ^{13}CNMR (100 MHz, chloroform-d) spectra of **S10** monomer at 298K.

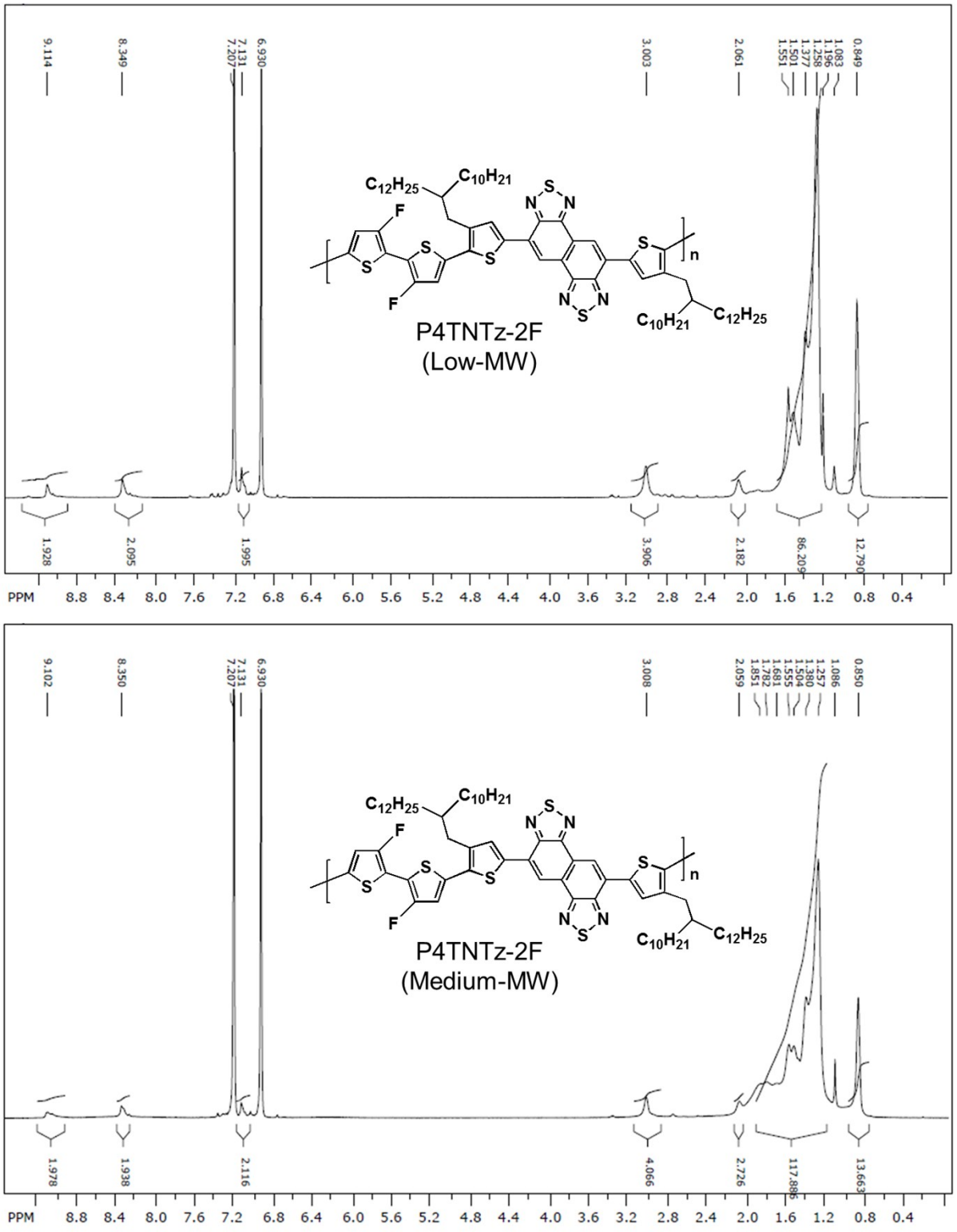

Fig. S7 ^{1}H NMR (500 MHz, *o*-dichlorobenzene-d4) spectra of P4TNTz-2F at 383K.

Fig. S8 Thermogravimetric analysis (TGA) plots of P4TNTz-2F (with different molecular weights) and P4T2FBT-2F.

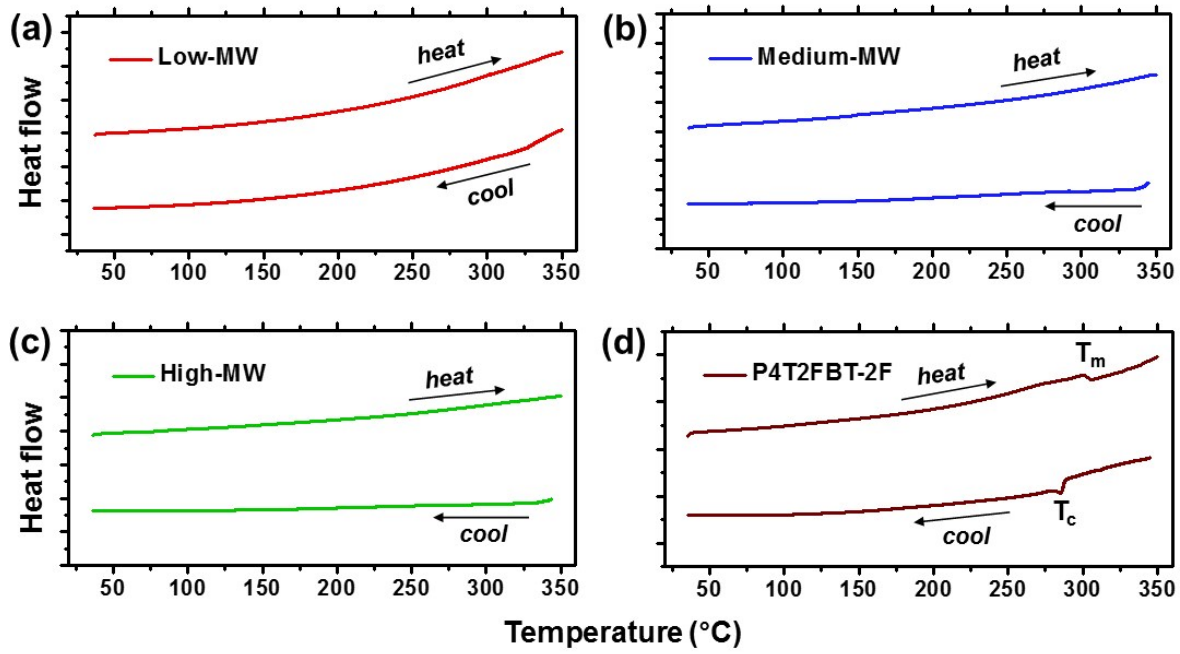

Fig. S9 Differential scanning calorimetry (DSC) of P4TNTz-2F (with different molecular weights) and P4T2FBT-2F.

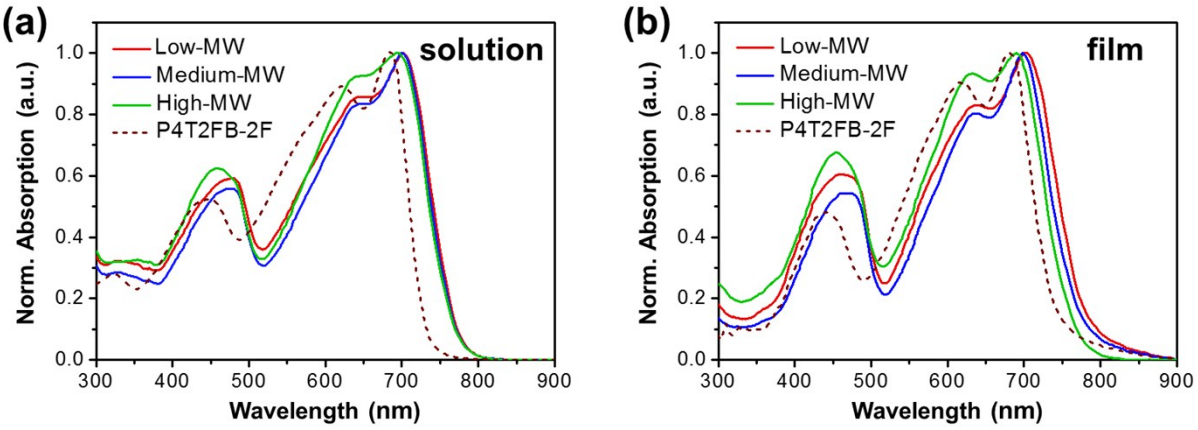

Fig. S10 UV-vis absorption spectra of P4TNTz-2F (with different molecular weights) and P4T2FBT-2F (a) in CB at a concentration of 0.025 g L^{-1} for 25 °C and (b) as thin films prepared by CB.

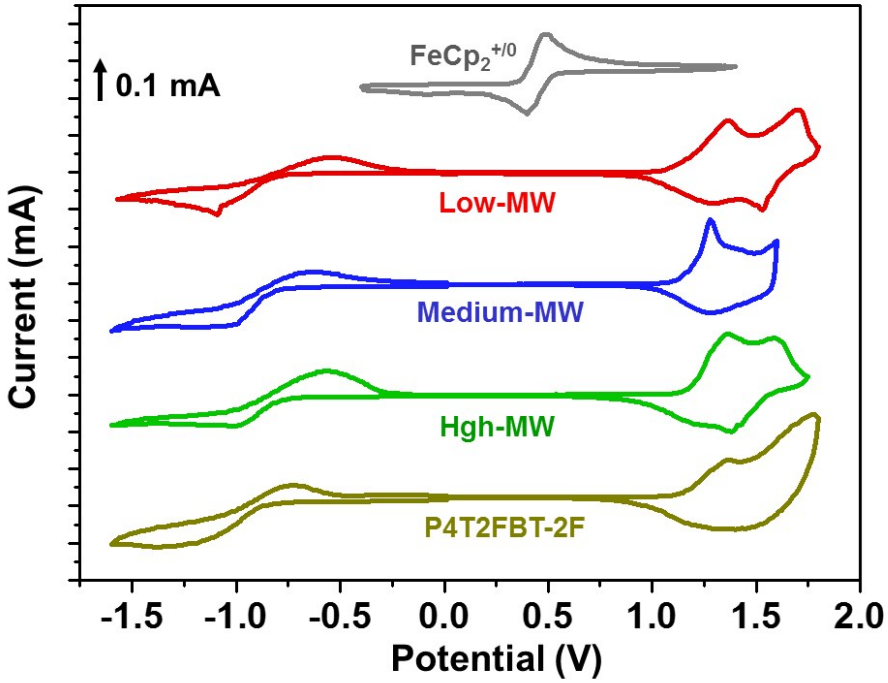

Fig. S11 Cyclic voltammograms (CV) of P4TNTz-2F (with different molecular weights) and P4T2FBT-2F.

Table S2 Properties of P4TNTz-2F as a function of molecular weight and P4T2FBT-2F.

Materials	T_d [°C][a]	$\lambda_{max}^{solution}$ [nm][b]	λ_{max}^{film} [nm][b]	$E_g^{solution}$ [eV][c]	E_g^{film} [eV][d]	E_{HOMO}^{CV} [eV][e]	E_{LUMO}^{CV} [eV][e]	E_{LUMO}^{opt} [eV][f]
Low-MW	429.9	478, 643, 701	462, 638, 701	1.62	1.59	-5.46	-3.56	-3.87
Medium-MW	429.7	475, 642, 699	462, 636, 697	1.62	1.61	-5.46	-3.55	-3.86
High-MW	435.5	458, 641, 694	455, 632, 690	1.62	1.63	-5.47	-3.55	-3.85
P4T2FBT-2F	420.6	442, 619, 682	440, 617, 681	1.68	1.67	-5.47	-3.51	-3.80

a) Thermal decomposition temperature corresponding to 5% weight loss determined by TGA. b) From solution in CB and thin films on glass substrates. c) Energy gaps for solution and d) optical band gaps for solid state calculated from the absorption edges. e) Calculated from the onsets of oxidation and reduction potential measured by CV. f) The LUMO energy levels were estimated from the HOMO energy levels (CV) and the optical band gaps (UV-vis) in the solid state by using the following equation: $E_{LUMO} = E_g^{opt} + E_{HOMO}$.[5]

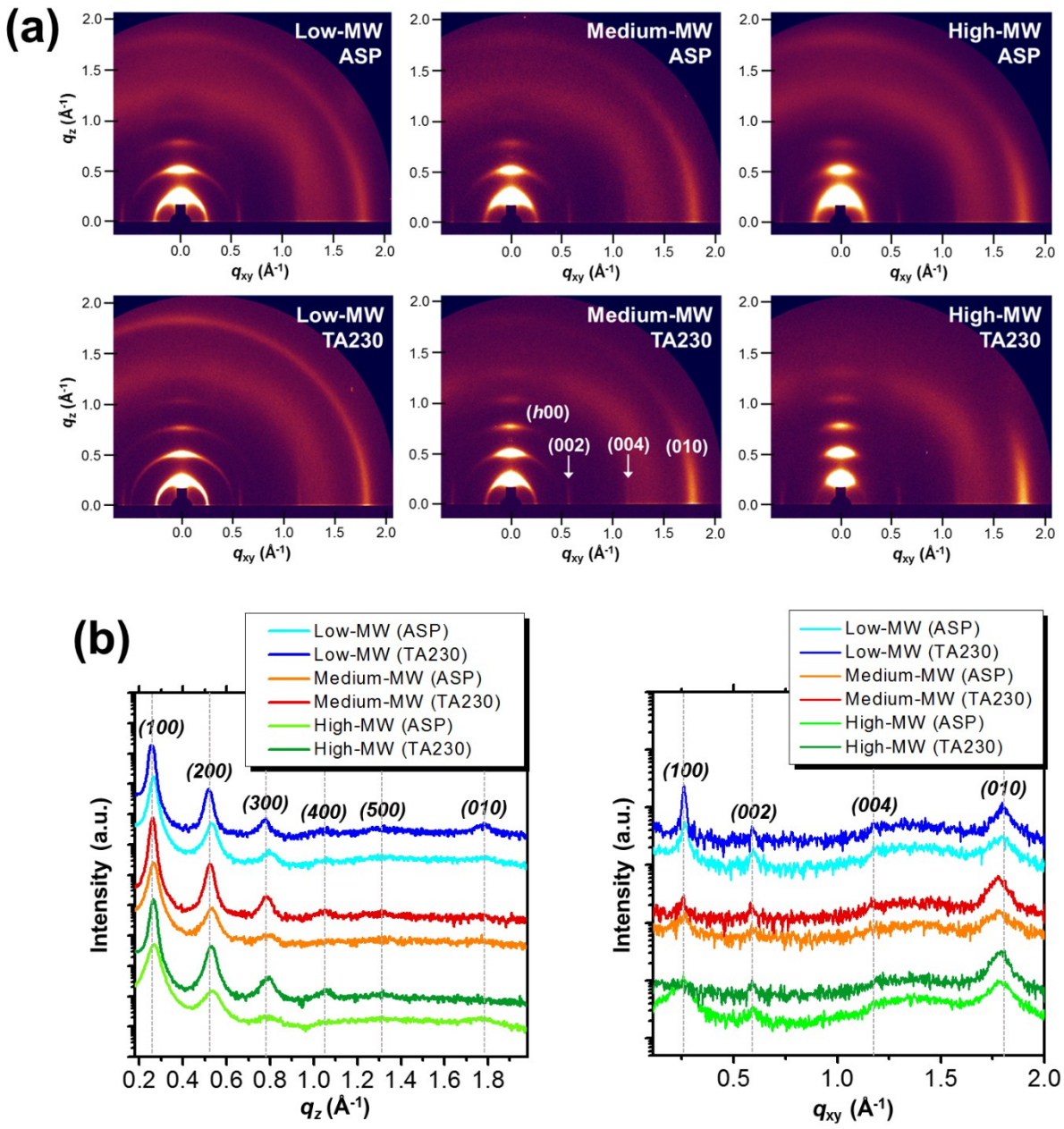

Fig. S12 (a) 2D GIXD images of P4TNTz-2F films prepared from CB as as-spun (top row) and thermally annealed at 230 °C (bottom row). (b) The corresponding GIXD diffractogram profiles along the out-of-plane (left row) and in-plane (right row) directions.

Table S3 Crystallographic information of P4TNTz-2F thin films. The coherence length is determined from the fullwidth-at-half-maximum (FWHM) of X-ray diffraction. N/A denotes not available.

	Crystallographic parameters			Low-MW	Medium-MW	High-MW
As-spun	Edge-on	Lamellar packing (100)	q (Å^{-1})	0.2640	0.2650	0.2661
			d-spacing (Å)	23.80	23.71	23.61
			FWHM (Å^{-1})	0.0266	0.0293	0.0412
			Coherence length (Å)	236.48	214.59	152.58
		π-π stack (010)	q (Å^{-1})	1.7946	1.7779	1.7812
			d-spacing (Å)	3.50	3.53	3.53
			FWHM (Å^{-1})	0.1266	0.1260	0.1229
			Coherence length (Å)	49.63	49.87	51.12
	Face-on	Lamellar packing (100)	q (Å^{-1})	0.2581	0.2665	0.2613
			d-spacing (Å)	24.34	23.58	24.04
			FWHM (Å^{-1})	0.0341	0.0442	0.0948
			Coherence length (Å)	184.42	142.06	66.26
		π-π stack (010)	q (Å^{-1})	N/A	N/A	N/A
			d-spacing (Å)	N/A	N/A	N/A
			FWHM (Å^{-1})	N/A	N/A	N/A
			Coherence length (Å)	N/A	N/A	N/A
	Backbone direction (002)		q (Å^{-1})	0.5901	0.5868	0.5936
			d-spacing (Å)	10.65	10.71	10.59
			FWHM (Å^{-1})	0.0397	0.0349	0.0317
			Coherence length (Å)	158.11	179.88	198.40
TA230	Edge-on	Lamellar packing (100)	q (Å^{-1})	0.2557	0.2599	0.2640
			d-spacing (Å)	24.57	24.52	23.80
			FWHM (Å^{-1})	0.0242	0.0199	0.0234
			Coherence length (Å)	260.17	316.06	268.86
		π-π stack (010)	q (Å^{-1})	1.7914	1.7743	1.7881
			d-spacing (Å)	3.51	3.54	3.51
			FWHM (Å^{-1})	0.0913	0.0955	0.0943
			Coherence length (Å)	68.84	65.80	66.63
	Face-on	Lamellar packing (100)	q (Å^{-1})	0.2581	0.2562	N/A
			d-spacing (Å)	24.34	24.52	N/A
			FWHM (Å^{-1})	0.0185	0.0154	N/A

			Coherence length (Å)	340.18	408.26	N/A
		π-π stack (010)	q (Å^{-1})	1.8029	N/A	N/A
			d-spacing (Å)	3.49	N/A	N/A
			FWHM (Å^{-1})	0.0825	N/A	N/A
			Coherence length (Å)	76.21	N/A	N/A
	Backbone direction (002)		q (Å^{-1})	0.5885	0.5833	0.5868
			d-spacing (Å)	10.68	10.77	10.71
			FWHM (Å^{-1})	0.0243	0.0300	0.0302
			Coherence length (Å)	258.46	209.65	207.91

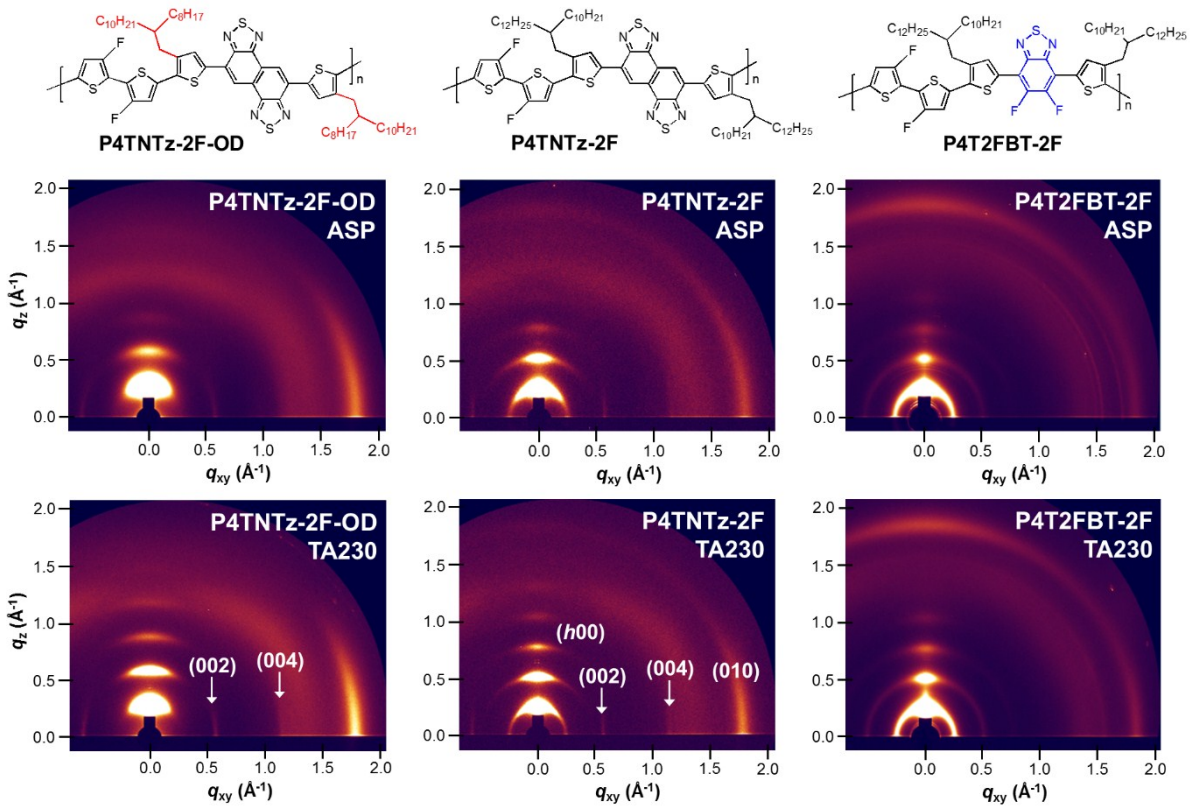

Fig. S13 2D GIXD images of P4TNTz-2F-OD, P4TNTz-2F, and P4T2FBT-2F films prepared from CB as as-spun (top row) and thermally annealed at 230 °C (bottom row).

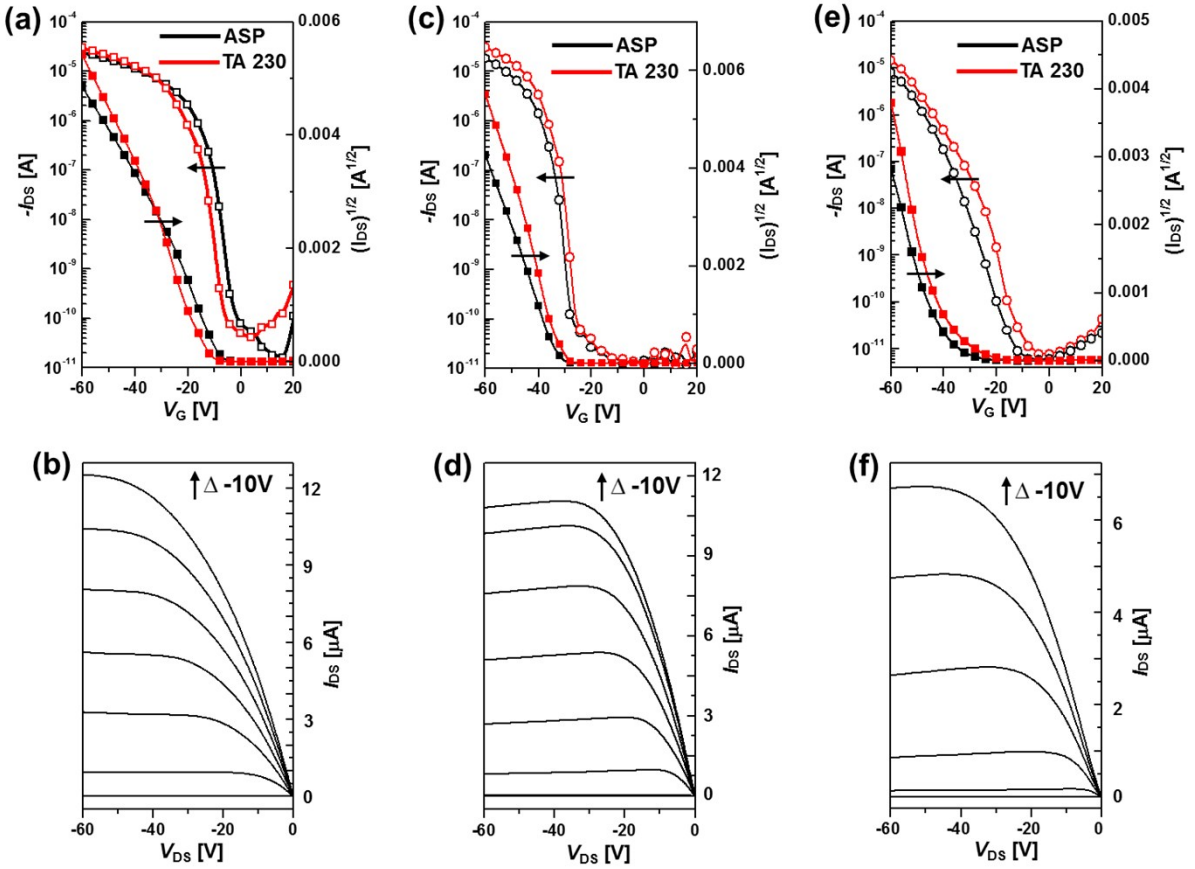

Fig. S14 PFET transfer curves (top row) and output curves (bottom row) for P4TNTz-2F based on (a, b) low-MW, (c, d) medium-MW, and (e, f) high-MW, respectively.

Table S4 PFET mobility of P4TNTz-2F as a function of molecular weight.

Polymer	Thermal Annealing	μ_h ($cm^2\ V^{-1}\ s^{-1}$)	$I_{on}/\ I_{off}$	V_{th}
Low-MW	-	0.28	4.6×10^5	-8.4
	TA230	0.52	7.3×10^5	-1.5
Medium-MW	-	0.40	1.1×10^6	-3.3
	TA230	1.07	1.2×10^7	-3.2
High-MW	-	0.42	4.2×10^5	-4.2
	TA230	0.89	1.8×10^7	-4.1

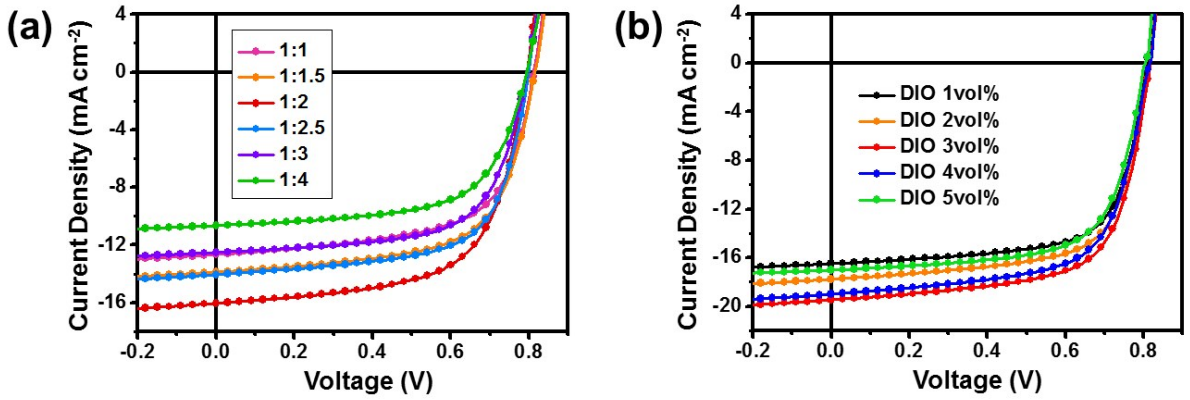

Fig. S15 *J–V* characteristics of M-MW P4TNTz-2F:$PC_{71}BM$ PSCs (a) without DIO (for various D:A ratio) and (b) with various DIO vol%.

Table S5 The detailed photovoltaic performances of the solar cells based on M-MW P4TNTz-2F:$PC_{71}BM$ with different D:A ratio and DIO vol%.

D:A Ratio	DIO [vol%]	V_{OC} [V]	J_{SC} [mA cm^{-2}]	FF [%]	PCE_{max} (PCE_{ave}) [a] [%]
1:1	–	0.82	12.65	62.3	6.47 (6.29 ± 0.16)
1:1.5	–	0.83	13.84	62.6	7.20 (7.01 ± 0.18)
1:2	–	0.80	16.04	62.8	8.07 (7.93 ± 0.14)
1:2.5	–	0.80	14.04	65.5	7.36 (7.09 ± 0.23)
1:3	–	0.80	12.52	64.2	6.44 (6.20 ± 0.22)
1:4	–	0.80	10.64	62.6	5.34 (5.21 ± 0.12)
1:2	1	0.81	16.50	68.6	9.17 (9.03 ± 0.11)
1:2	2	0.82	17.76	67.0	9.77 (9.44 ± 0.32)
1:2	3	0.82	19.45	66.5	10.62 (10.33 ± 0.24)
1:2	4	0.81	18.99	65.9	10.14 (9.84 ± 0.27)
1:2	5	0.80	17.00	67.5	9.18 (8.96 ± 0.19)
1:1.5	3	0.84	15.95	65.1	8.73 (8.54 ± 0.17)
1:1.8	3	0.81	18.71	66.6	10.09 (9.81 ± 0.24)
1:2.2	3	0.81	19.40	65.3	10.27 (9.93 ± 0.31)
1:2.5	3	0.81	17.18	67.2	9.35 (9.12 ± 0.20)
1:3	3	0.82	16.05	61.2	8.05 (7.91 ± 0.13)

[a] The values in parentheses stand for the average PCEs with standard deviation from over 12 devices prepared without DIO treatment and over 16 devices prepared with DIO treatments.

Fig. S16 *J–V* characteristics of M-MW P4TNTz-2F:$PC_{71}BM$ PSCs prepared from (a) CB:DIO, (b) CB:CN, and (c) CB:DPE with different thicknesses.

Table S6 The detailed photovoltaic performances of the solar cells based on M-MW P4TNTz-2F:$PC_{71}BM$ as a function of solvents. The M-MW P4TNTz-2F:$PC_{71}BM$ ratio was 1:2 (wt:wt%).

Additive [vol%]	Spin rate [rpm]	Thickness [nm]	V_{OC} [V]	J_{SC} [mA cm^{-2}]	FF [%]	PCE_{max} (PCE_{ave}) [a] [%]
DIO (3)	1000	390	0.82	19.01	58.0	9.05 (8.84 ± 0.20)
	1200	365	0.83	19.92	62.0	10.25 (9.98 ± 0.23)
	1300	350	0.82	19.45	66.5	10.62 (10.33 ± 0.24)
	1500	325	0.81	18.47	67.3	10.06 (9.85 ± 0.18)
	1800	290	0.81	17.22	67.6	9.43 (9.20 ± 0.20)
	2000	260	0.82	15.51	65.7	8.36 (8.23 ± 0.12)
CN (3)	800	-	0.82	16.32	58.2	7.79 (7.45 ± 0.28)
	1200	-	0.82	17.08	59.8	8.38 (8.02 ± 0.31)
	1500	-	0.82	15.32	63.7	8.10 (7.88 ± 0.19)
	2000	-	0.82	14.75	66.2	8.01 (7.69 ± 0.28)
DPE (3)	800	-	0.81	16.67	59.4	8.03 (7.85 ± 0.16)
	1200	-	0.81	17.42	61.5	8.68 (8.43 ± 0.22)
	1500	-	0.82	15.42	65.9	8.34 (8.18 ± 0.12)
	2000	-	0.82	13.88	66.8	7.61 (7.44 ± 0.15)

[a] The values in parentheses stand for the average PCEs with standard deviation from over 16 devices for DIO additive and over 8 devices for CN and DPE additives.

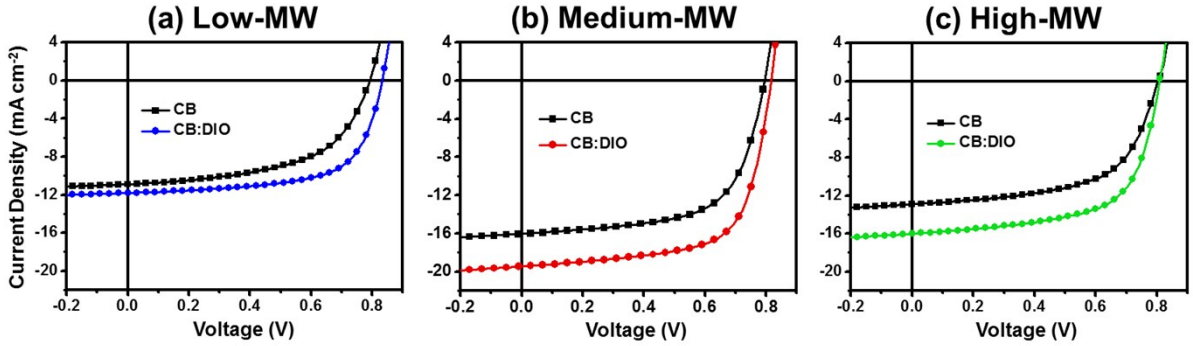

Fig. S17 *J–V* characteristics of P4TNTz-2F:$PC_{71}BM$ PSCs prepared from CB and CB:DIO as a function of molecular weights.

Table S7 The detailed photovoltaic performances of the solar cells based on P4TNTz-2F:$PC_{71}BM$ as a function of molecular weights.

Molecular weight	Spin rate [rpm]	Thickness [nm]	DIO [vol%]	V_{OC} [V]	J_{SC} [mA cm^{-2}]	FF [%]	PCE_{max} (PCE_{ave}) [a] [%]
Low-MW	1000	125	-	0.80	10.89	54.8	4.78 (4.64 ± 0.12)
	800	150	3	0.83	11.32	65.2	6.12 (5.85 ± 0.24)
	1000	130	3	0.84	11.80	64.3	6.37 (6.15 ± 0.19)
	1300	115	3	0.84	10.82	67.0	6.09 (5.91 ± 0.15)
	1500	100	3	0.84	10.66	65.2	5.84 (5.71 ± 0.09)
Medium-MW	1300	345	-	0.82	16.50	57.8	7.82 (7.63 ± 0.17)
	1500	320	-	0.80	16.04	62.8	8.07 (7.93 ± 0.14)
	1800	280	-	0.80	15.33	63.1	7.74 (7.59 ± 0.11)
	2000	250	-	0.83	12.43	64.6	6.75 (6.55 ± 0.16)
	1300	350	3	0.82	19.45	66.5	10.62 (10.33 ± 0.24)
	1500	325	3	0.81	18.47	67.3	10.06 (9.85 ± 0.18)
High-MW	1800	355	-	0.82	12.40	56.2	5.71 (5.41 ± 0.27)
	2000	330	-	0.81	12.91	59.1	6.18 (5.85 ± 0.30)
	2500	280	-	0.81	11.73	63.2	6.01 (5.71 ± 0.24)
	1500	410	3	0.81	16.30	58.9	7.77 (7.53 ± 0.21)
	1800	365	3	0.81	16.02	63.4	8.22 (7.87 ± 0.32)
	2000	335	3	0.81	15.66	62.8	7.96 (7.68 ± 0.26)
	2500	285	3	0.82	13.20	65.0	7.03 (6.91 ± 0.10)

[a] The values in parentheses stand for the average PCEs with standard deviation from over 12 devices.

Table S8 Short circuit current density (J_{SC}) and calculated J_{SC} from the EQE spectrum of OPV devices for the M-MW P4TNTz-2F:$PC_{71}BM$ prepared from CB without DIO and with DIO.

D:A	Additive	J_{SC} [mA cm^{-2}]	$J_{SC\ (cal.)}$ [mA cm^{-2}]
M-MW:$PC_{71}BM$	-	16.04	15.89
	DIO (3 vol%)	19.45	18.86

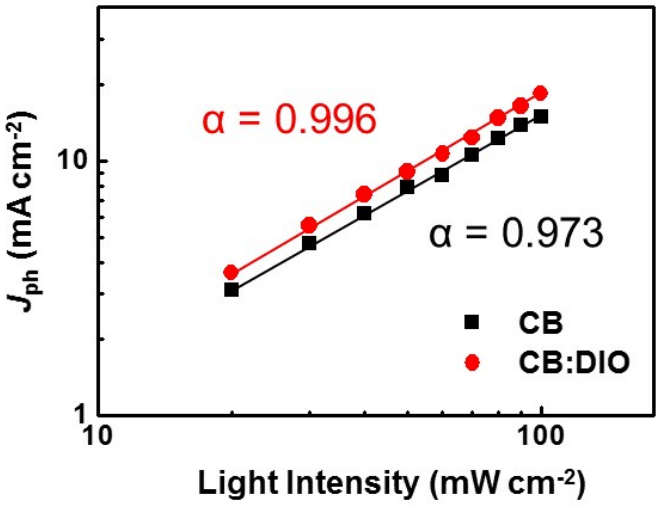

Fig. S18 J_{ph} dependence on light intensity of optimum devices for the P4TNTz-2F (M-MW):$PC_{71}BM$ prepared from different solvents.

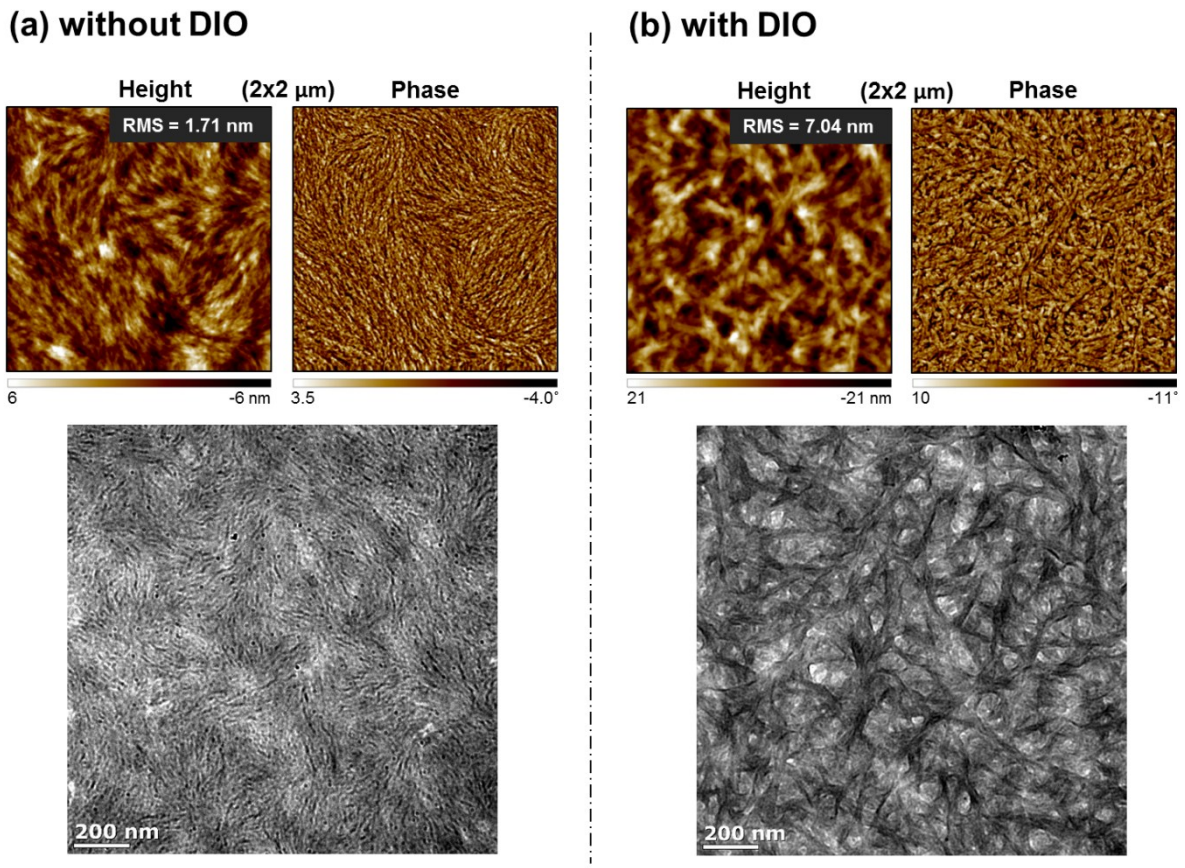

Fig. S19 TM-AFM topography images and phase images, TEM images of M-MW P4TNTz-2F thin films prepared from CB without DIO and with 3 vol% DIO.

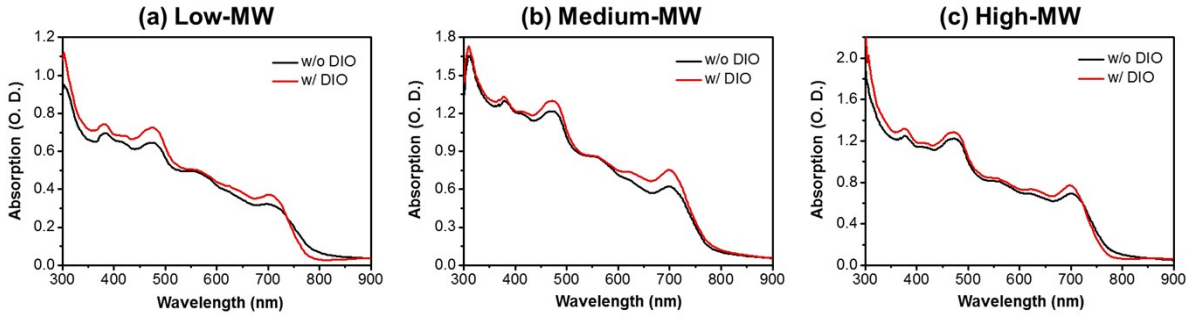

Fig. S20 UV-vis absorption spectra of P4TNTz-2F:$PC_{71}BM$ blend films prepared from CB without DIO and with DIO (3 vol%) for (a) L-MW, (b) M-Mw, and (c) H-MW.

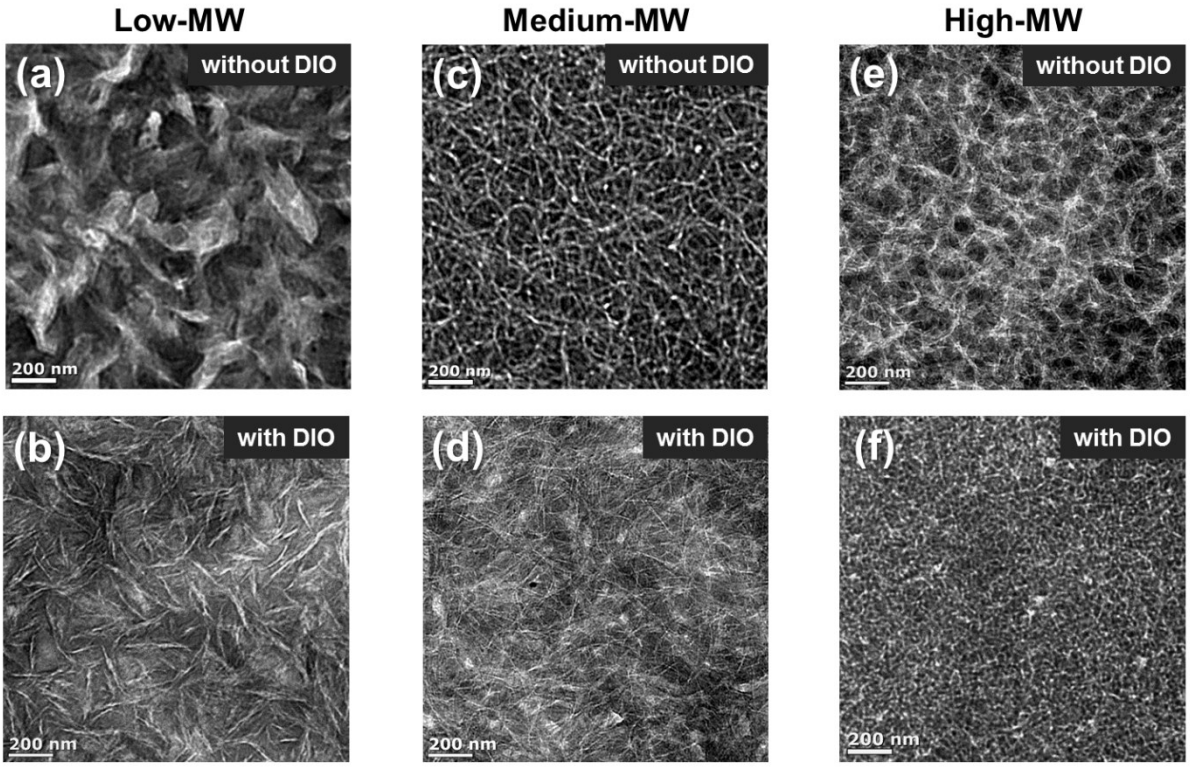

Fig. S21 TEM images of P4TNTZ-2F(as a function of molecular weights):$PC_{71}BM$ blend films on the actual optimum devices prepared from CB without DIO (a, c, and e) and with 3 vol% DIO (b, d, and f) under same film-forming condition (≈70 ˚C). Using bright-field TEM, we find that the large-scale morphology of P4TNTz-2F BHJs processed by pure CB changes drastically when the M_n is increased (top row). Large domains (bright-colored) have been observed in other D-A polymer:fullerene BHJs and are generally identified as polymer-rich domains because fullerenes have a higher electron density than most D-A polymers and scatter electrons more strongly, leading to dark-colored features.[11] Increasing the M_n of P4TNTz-2F prevents polymer-rich domains from forming in these BHJs. It has recently been reported that the fibril width is correlated with the polymer solubility; generally, the narrower fibrils are obtained from less soluble polymer in organic solvents.[12,13] Hence, as the M_n increases, the reason for narrower fibril formation in the blend films is probably due to lower solubility of polymer in CB. Using DIO, the BHJ films possess reduced polymer domains and distinct polymer:fullerene phase separation, and the M-MW BHJ films showed polymer nanowire structures. Although the BHJ films based on H-MW P4TNTz-2F formed smaller polymer domains than the BHJ films based on L-MW P4TNTz-2F, the film thicknesses were formed over 400 nm under same film-forming condition (≈70 ˚C, 1000 rpm) due to its low solubility, leading to be detrimental for FF and PCE of PSCs.

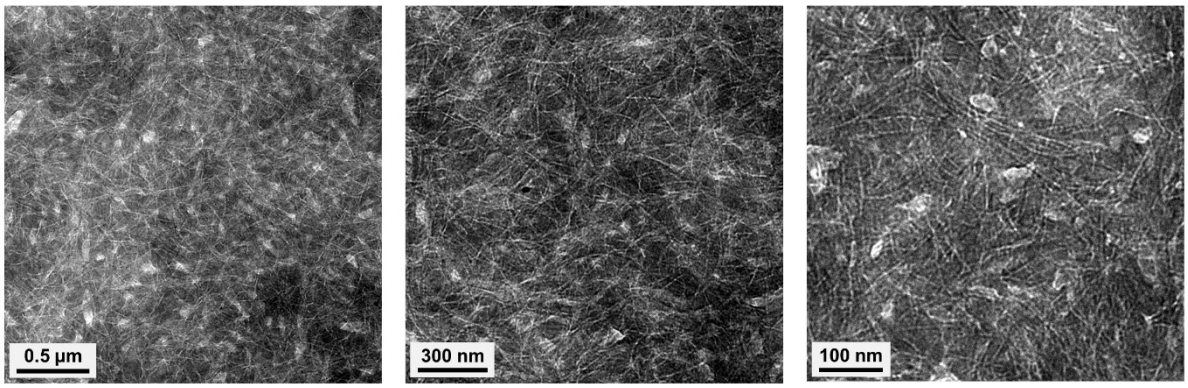

Fig. S22 TEM images of M-MW P4TNTz-2F:$PC_{71}BM$ blend films prepared from CB with 3 vol% DIO.

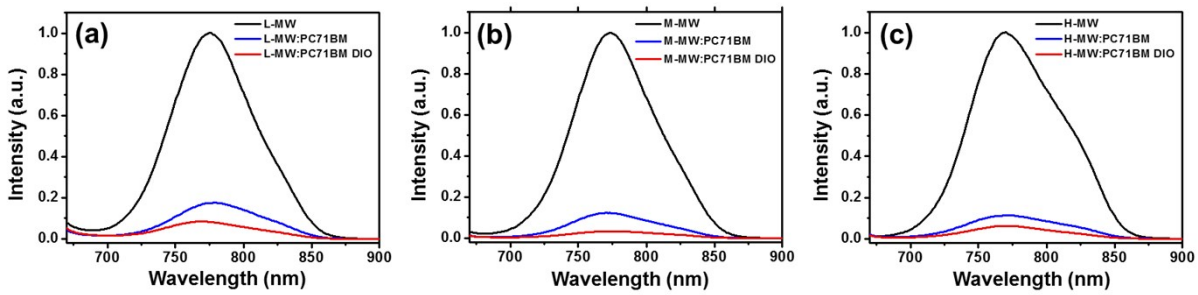

Fig. S23 Photoluminescence spectra of P4TNTz-2F:$PC_{71}BM$ blend films, based on (a) L-MW, (b) M-MW, and (c) H-MW, without DIO and with DIO (3 vol%). The films were excited with 697 nm wavelength. Each spectrum was corrected for the absorption of the film at the excitation wavelength. In L-MW P4TNTz-2F BHJs without DIO, large scale D/A phase separation are clearly visible, and when the M_n is increased, the size of these phase separation decreases (Fig. S21). Macrophase separation in the L-MW P4TNTz-2F blend film without DIO limits the probability for exciton dissociation by reducing donor/acceptor interfaces, leading to a relatively poor PL quenching efficiency.

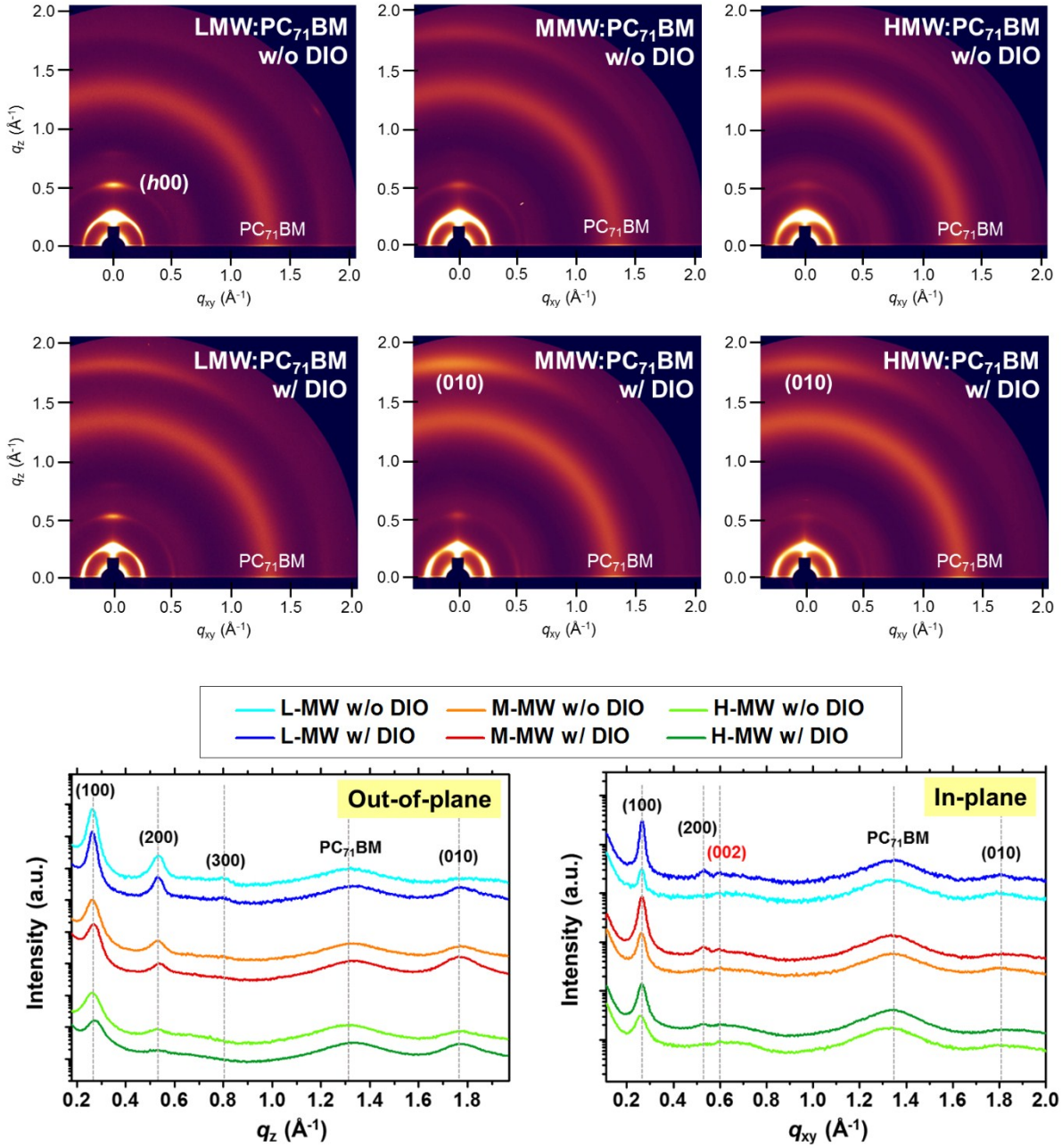

Fig. S24 2D GIXD images of P4TNTz-2F:$PC_{71}BM$ blend films prepared from CB without DIO (w/o DIO, top row) and with 3 vol% DIO (w/ DIO, bottom row). The corresponding GIXD diffractogram profiles along the out-of-plane (left row) and in-plane (right row) directions.

Table S9 Crystallographic information of P4TNTz-2F:$PC_{71}BM$ blend films prepared from CB and CB:DIO.

	Crystallographic parameters			Low-MW	Medium-MW	High-MW
CB	Edge-on	Lamellar packing (100)	*q* (Å^{-1})	0.2633	0.2633	0.2644
			d-spacing (Å)	23.86	23.86	23.76
		π-π stack (010)	*q* (Å^{-1})	1.7946	1.7910	1.7946
			d-spacing (Å)	3.50	3.51	3.50
	Face-on	Lamellar packing (100)	*q* (Å^{-1})	0.2638	0.2638	0.2581
			d-spacing (Å)	23.82	23.82	24.34
		π-π stack (010)	*q* (Å^{-1})	1.7584	1.7730	1.7730
			d-spacing (Å)	3.57	3.54	3.54
	Backbone direction (002)		*q* (Å^{-1})	0.5995	0.6036	0.5995
			d-spacing (Å)	10.48	10.41	10.48
CB:DIO	Edge-on	Lamellar packing (100)	*q* (Å^{-1})	0.2630	0.2712	0.2762
			d-spacing (Å)	23.89	23.16	22.75
		π-π stack (010)	*q* (Å^{-1})	1.8023	1.7987	1.7965
			d-spacing (Å)	3.49	3.49	3.50
	Face-on	Lamellar packing (100)	*q* (Å^{-1})	0.2650	0.2651	0.2638
			d-spacing (Å)	23.71	23.70	23.82
		π-π stack (010)	*q* (Å^{-1})	1.7657	1.7765	1.7766
			d-spacing (Å)	3.56	3.54	3.54
	Backbone direction (002)		*q* (Å^{-1})	0.5918	0.5955	0.5995
			d-spacing (Å)	10.62	10.55	10.48

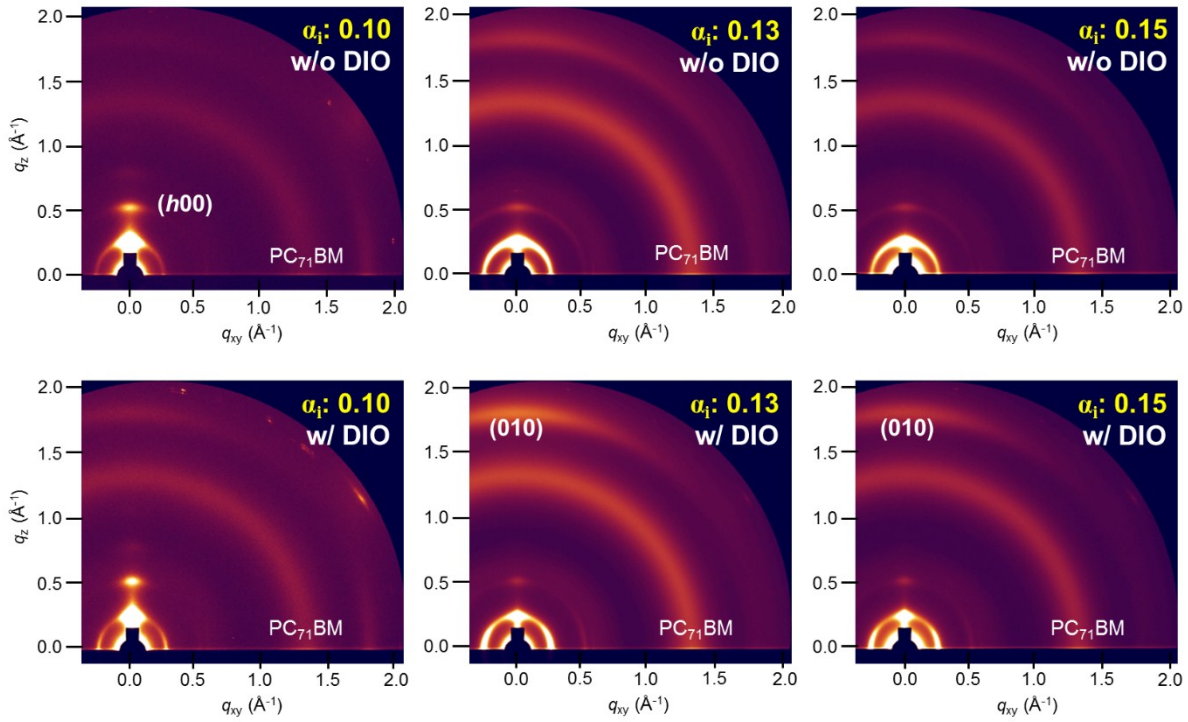

Fig. S25 2D GIXD images of M-MW P4TNTz-2F:$PC_{71}BM$ blend films prepared from CB without DIO (w/o DIO, top row) and with 3 vol% DIO (w/ DIO, bottom row) with different incident angles (α_i = 0.10, 0.13, and 0.15).

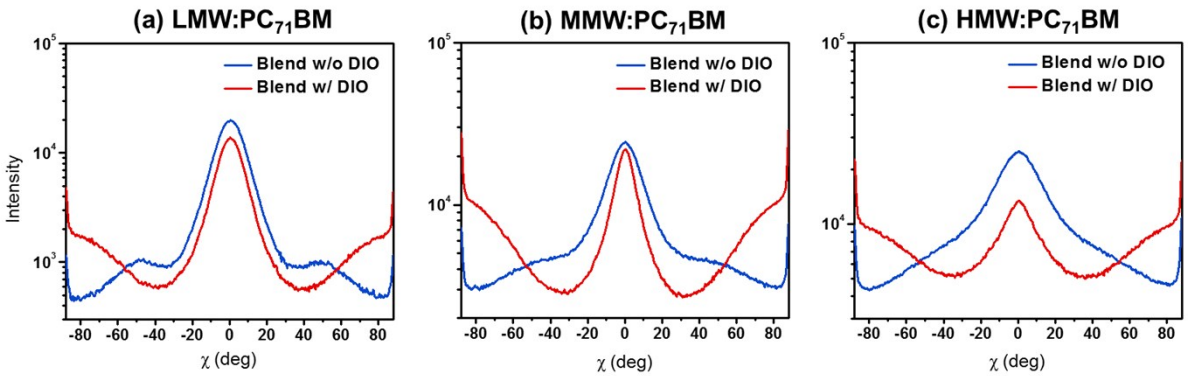

Fig. S26 Pole figures extracted from the lamellar diffraction for the blend films based on different molecular weights of P4TNTz-2F.

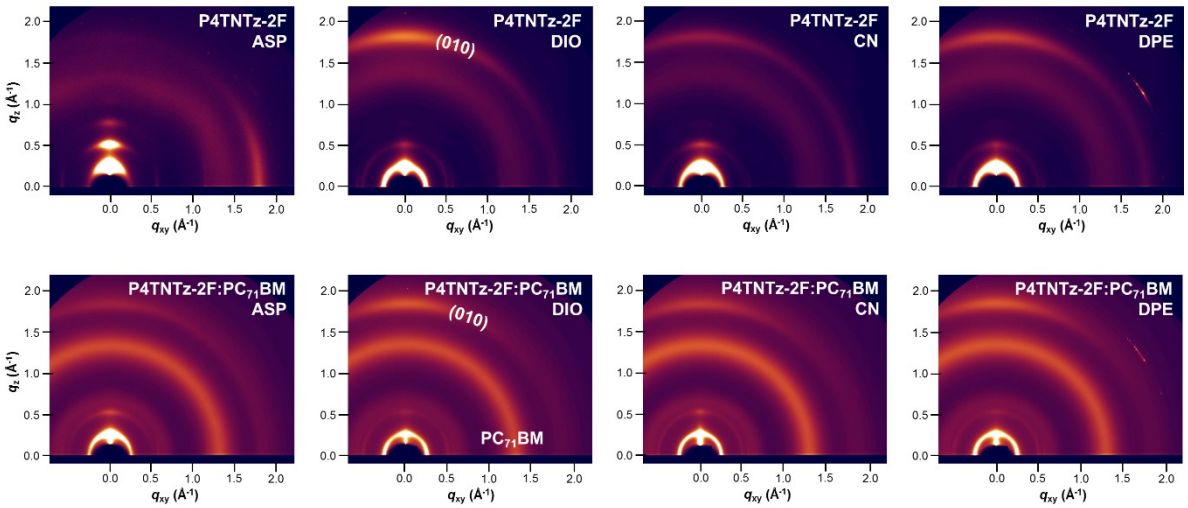

Fig. S27 2D GIXD images of P4TNTz-2F neat films (top row) and P4TNTz-2F:$PC_{71}BM$ blend films (bottom row) prepared from CB with various additives.

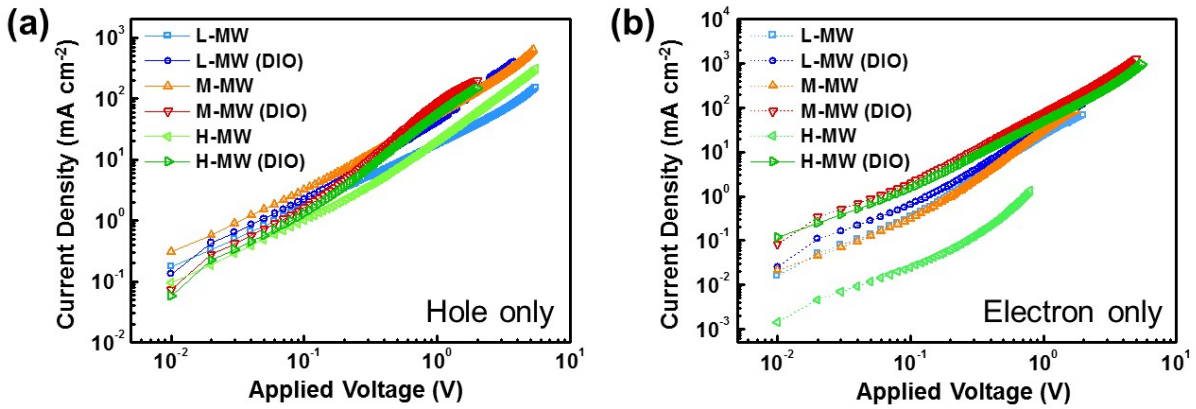

Fig. S28 Dark current density versus effective voltage characteristics of a) hole-only devices and b) electron only devices, with photoactive layers based on P4TNTz-2F:$PC_{71}BM$ blends without and with DIO (3 vol%).

Table S10. Mobility results of space charge limited current (SCLC) devices based on P4TNTz-2F:$PC_{71}BM$ prepared from CB without DIO and with DIO (3 vol%).

D:A	solvent	μ_h [$cm^2\ V^{-1}\ s^{-1}$]	μ_e [$cm^2\ V^{-1}\ s^{-1}$]	μ_h/μ_e
Low-MW:$PC_{71}BM$	CB	4.53×10^{-4}	2.13×10^{-3}	0.21
	CB:DIO	3.47×10^{-3}	3.19×10^{-3}	1.09
Medium-MW:$PC_{71}BM$	CB	1.98×10^{-3}	2.77×10^{-3}	0.71
	CB:DIO	8.31×10^{-3}	4.53×10^{-3}	1.83
High-MW:$PC_{71}BM$	CB	8.94×10^{-4}	1.23×10^{-4}	7.27
	CB:DIO	5.90×10^{-3}	2.46×10^{-3}	2.40

Supplementary References

1 J. W. Jo, J. W. Jung, H.-W. Wang, P. Kim, T. P. Russell and W. H. Jo, *Chem. Mater.*, 2014, **26**, 4214.

2 I. Osaka, M. Shimawaki, H. Mori, I. Doi, E. Miyazaki, T. Koganezawa and K. Takimiya, *J. Am. Chem. Soc.*, 2012, **134**, 3498.

3 J. Lu, F. Liang, N. Drolet, J. Ding, Y. Tao and R. Movileanu, *Chem. Commun.*, 2008, 5315.

4 Z. Chen, P. Cai, J. Chen, X. Liu, L. Zhang, L. Lan, J. Peng, Y. Ma and Y. Cao, *Adv. Mater.*, 2014, **26**, 2586.

5 H. Zhou, L. Yang, A. C. Stuart, S. C. Price, S. Liu and W. You, *Angew. Chem. Int. Ed.*, 2011, **50**, 2995.

6 M. J. Frisch, *et al*. *Gaussian 09, Revision A.02*, Gaussian, Inc., Wallingford CT, **2009**.

7 Y. X. Xu, C. C. Chueh, H. L. Yip, F. Z. Ding, Y. X. Li, C. Z. Li, X. Li, W. C. Chen and A. K. Y. Jen, *Adv. Mater.*, 2012, **24**, 6356.

8 G. Horowitz, *Adv. Mater.*, 1998, **10**, 365.

9 S. B. Jo, J. H. Lee, M. Sim, M. Kim, J. H. Park, Y. S. Choi, Y. Kim, S.-G. Ihn, and K. Cho, *Adv. Energy Mater.*, 2011, **1**, 690.

10 M. A. Lampert and P. Mark, *Current Injection in Solids*, Academic Press, New York 1970.

11 J. A. Bartelt, J. D. Douglas, W. R. Mateker, A. E. Labban, C. J. Tassone, M. F. Toney, J. M. J. Fréchet, P. M. Beaujuge and M. D. McGehee, *Adv. Energy Mater*., 2014, **4**, 1301733.

12 W. Li, K. H. Hendriks, A. Furlan, W. S. C. Roelofs, S. C. J. Meskers, M. M. Wienk and R. A. J. Janssen*, Adv. Mater.*, 2014, **26**, 1565.

13 W. Li, K. H. Hendriks, A. Furlan, W. S. C. Roelofs, M. M. Wienk and R. A. J. Janssen, *J. Am. Chem. Soc.*, 2013, **135**, 18942.